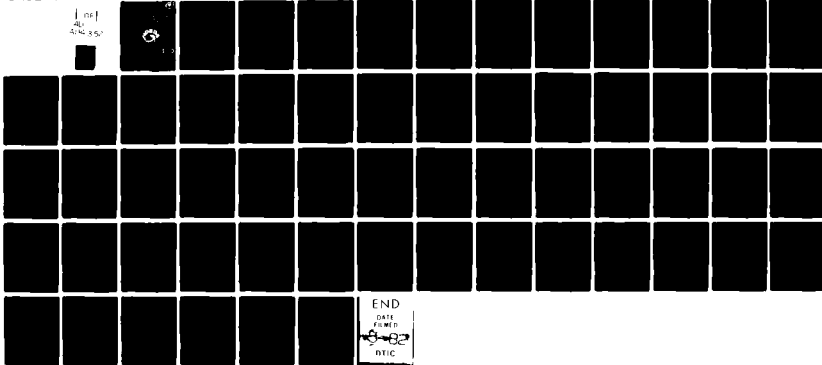


AD-A114 352

NAVAL OCEAN RESEARCH AND DEVELOPMENT ACTIVITY NSTL S--ETC F/0 8/3
THE DYNAMICS OF THE LOOP CURRENT AND SHED EDDIES IN A NUMERICAL--ETC(U)
OCT 81 H E HURLBURT, J D THOMPSON
NORDA-TN-125

NL

UNCLASSIFIED



END

DATA

FILED

10-82

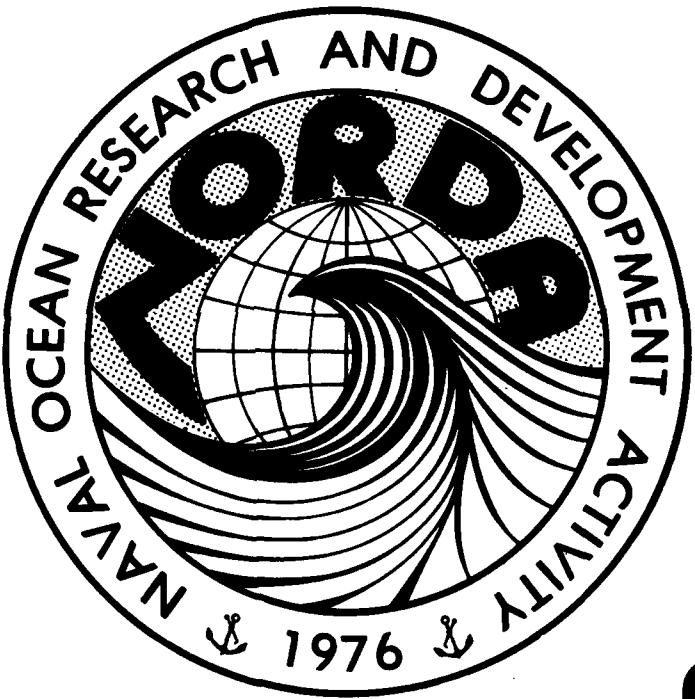
RTIC

9

NORDA Technical Note 125

Naval Ocean Research
and Development Activity
NSTL Station, Mississippi 39529

The Dynamics of the Loop Current and Shed Eddies in a Numerical Model of the Gulf of Mexico



DTIC
SELECTED
MAY 13 1982

Harley E. Hurlburt
J. Dana Thompson

Numerical Modeling Division
Ocean Science and Technology Laboratory

October 1981

82 05-10 013

DISTRIBUTION STATEMENT A
Approved for public release;
Distribution Unlimited

DTIC FILE COPY

THE DYNAMICS OF THE LOOP CURRENT AND SHED
EDDIES IN A NUMERICAL MODEL OF THE GULF OF MEXICO

Harley E. Hurlburt
J. Dana Thompson

October 1981

Environmental Simulation Branch
Code 322
Naval Ocean Research and Development Activity
NSTL Station, MS 39529

To appear in

Nihoul, J. C. J. (editor), 1982: Hydrodynamics of Semi-enclosed Seas.
Elsevier Scientific Publishing Company, Amsterdam (in press).

Accession For	
NTIS GRA&I	<input checked="" type="checkbox"/>
DTIC TAB	<input type="checkbox"/>
Unannounced	<input type="checkbox"/>
Justification	
By _____	
Distribution/ _____	
Availability Codes	
Dist	Avail and/or Special
A	



CONTENTS

Abstract	1
1. Introduction	2
2. Design of the numerical models and numerical experiments	3
3. An attempt to simulate the eddy shedding by the Loop Current	7
4. A simple test for the instability mechanism	9
5. CAV trajectories and Rossby wave theory	10
elucidate the Loop Current - eddy shedding dynamics	
5.1 CAV trajectory analysis	10
5.2 Influence of Rossby waves	12
5.3 Two time scales associated with the eddy shedding	14
5.4 Hypothesis testing	16
5.5 Eddy diameter, Loop Current penetration, and latitude of westward bending	16
5.6 Tests of some dynamical hypothesis	17
6. Regimes for the Loop Current in the reduced gravity model	20
6.1 The eddy-shedding regime (E)	20
6.2 The steady westward spreading regime (W)	20
6.3 The steady source-sink regime (N)	20
6.4 Stability regime diagram	23
7. Prevention of eddy shedding by topography and deep-water inflow through the Yucatan Straits	25
8. Barotropic vs. baroclinic instability and the important role of topography	28
8.1 Eddy-mean energetics	28
8.2 Kinetic energy vs. time	33
8.3 Modon generation in the barotropically unstable experiments	35
8.4 Flow characteristics associated with baroclinic instability	41
8.5 Flow characteristics of a mixed instability	43
9. Summary and Conclusions	46
Acknowledgements	47
Appendix A - List of symbols	47
Appendix B - New reduced gravity experiments for the regime diagram	49
Appendix C - Derivation of eddy-mean energetics for a two-layer, free-surface, primitive-equation model with open boundaries	49
References	55

THE DYNAMICS OF THE LOOP CURRENT AND SHED EDDIES IN A NUMERICAL MODEL OF THE GULF OF MEXICO

HARLEY E. HURLBURT and J. DANA THOMPSON

Environmental Simulation Branch (Code 322), Naval Ocean Research and Development Activity, NSTL Station, MS 39529 USA

ABSTRACT

The dynamics of the circulation in the Gulf of Mexico have been investigated using simple, efficient numerical models capable of simulating consistently observed dynamical features, including the Loop Current and the shedding of large anticyclonic eddies from the Loop. Over 150 model experiments were integrated to statistical equilibrium, typically 3-5 years.

One popular hypothesis holds that the Loop Current sheds anticyclonic eddies in response to annual variations in the inflow through the Yucatan Straits. However, a striking result from the models is their ability to simulate the observed quasi-annual eddy shedding period with no time variations in the inflow. The model-predicted eddy diameters, amplitudes, and westward propagation speeds are also realistic. The dominant instability mechanism in the eddy shedding is a horizontal shear instability of the first internal mode, a barotropic rather than a baroclinic instability. Therefore, a reduced-gravity model with one vertical mode is able to simulate the basic dynamics of the Loop Current-eddy system. Rossby-wave theory and a conservation of absolute vorticity trajectory analysis were used to explain the behavior of the Loop Current, including its northward penetration into the Gulf, the latitude of westward bending, the shedding period for the eddies, as well as their diameter, and their westward propagation speed.

A regime diagram for the reduced-gravity model was constructed in terms of the Reynolds number Re and the beta Rossby number $R_B = v_c / \beta L_p^2$, where v_c is the velocity at the core of the current, L_p is half the port separation distance and β is differential rotation. Eddy shedding can be prevented by reducing Re or by increasing R_B .

Bottom relief acts to inhibit baroclinic instability, yielding solutions more closely resembling those from the reduced-gravity model than the two-layer flat-bottom model. Topography also influences the paths of the shed eddies and, in the presence of sufficient deep water inflow through the Yucatan Straits, prevents Loop Current penetration, westward bending, and eddy shedding. In effect, the West Florida Shelf acts to reduce the port separation, increase R_B , and shift the Loop Current into a stable regime.

The signatures of barotropic and baroclinic instabilities in the two-layer Gulf of Mexico model were studied using upper and lower layer pressure fields and eddy-mean energetics. Both instability processes tend to drive a deep flow characterized by modon generation and they exhibit similar vertical phase relationships. However, in these experiments the westward propagation speeds associated with baroclinic instability are typically two to three times faster.

1. INTRODUCTION

Semi-enclosed seas are attractive domains for ocean modeling partly because they allow the use of numerical grids that resolve strong meandering currents and associated eddying phenomena also found in major ocean basins. The Gulf of Mexico is particularly attractive because it contains a major current system that sheds energetic anticyclonic eddies which are comparable in size to warm-core Gulf Stream rings. This system is illustrated in Fig. 1 by the depth of the 22°C isotherm in the eastern Gulf of Mexico based on a hydrographic survey by Liepper (1970). It shows the Loop Current entering from the south through the Yucatan Straits and exiting to the east through the Florida Straits. The mean transport through the straits is $\sim 30 \text{ m}^3/\text{s}$ (Nowlin, 1972). In Fig. 1 a large anticyclonic eddy is about to break-off from the Loop Current, as confirmed by subsequent observations (Elliott, 1979). The Loop Current penetrates into the Gulf and sheds these large anticyclonic eddies with a quasi-annual period. The eddies have a typical radius of 180 km and translate into the western Gulf at a mean speed of 2.4 cm/s (Elliott, 1979).

In this paper we present some basic dynamical ideas and numerical results concerning the behavior of the Loop Current-eddy system. The dynamical topics include 1) the nature of the instability associated with the eddy shedding, 2) the external and/or internal factors which determine the eddy shedding period, 3) the trajectory dynamics of the Loop Current and how they affect the penetration of the Loop into the Gulf, the eddy shedding, and the diameter of the eddies, 4) the existence of different regimes for the Loop Current, 5) two important roles of topography in the dynamics, and 6) the distinctive signatures of barotropic and baroclinic instability in the flow and in the energetics. Over 150 numerical experiments have been performed to explore the model parameter space, but more importantly to aid in the formulation and testing of dynamical hypotheses. This paper is both a distillation and an extension of Hurlburt and Thompson (1980), hereafter referred to as HT. That paper discusses the only previous numerical model of the Gulf of Mexico which was integrated to statistical equilibrium or which simulated the basic repetitive features of the eddy shedding by the Loop Current.

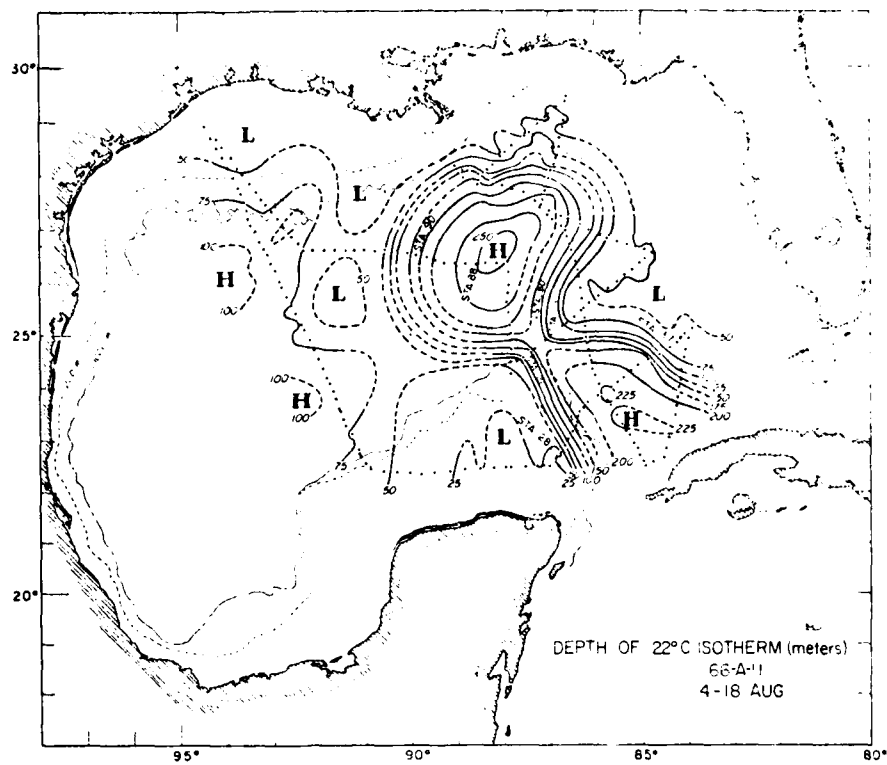


Fig. 1. Topography of the 22°C isothermal surface, 4-18 August 1966 (Alaminos cruise 66-A-11) from Leipper (1970). Subsequent data (Elliot, 1979) indicates that an anticyclonic eddy separated from the Loop Current within several months.

2. DESIGN OF THE NUMERICAL MODELS AND NUMERICAL EXPERIMENTS

The three numerical models of HT are used to elucidate the Loop Current-eddy shedding dynamics. These models were designed to be as simple as possible while retaining the ability to simulate the basic phenomena of interest. The three models are 1) reduced gravity, 2) barotropic, and 3) two-layer. The first two are mathematically identical except for parameter values, particularly the gravitational acceleration. The reduced gravity model is designed to represent the first internal mode and contains an upper active layer and a lower layer which is infinitely deep and at rest. In the reduced gravity and two-layer models the pycnocline is represented by an immiscible interface between two layers with a prescribed density contrast. In the reduced gravity model bottom topography and baroclinic instability are not permitted. Two active layers is the minimum to allow baroclinic instability and to allow coexistence of topography and the pycnocline. The barotropic and reduced gravity models demonstrate the behavior of the individual modes and provide

insight into how they interact in the two-layer model. They also allow the investigation of some phenomena in the simplest context.

The models are primitive equation on a β -plane and retain a free surface. Using the hydrostatic and Boussinesq approximations and a right-handed Cartesian coordinate system, the vertically integrated model equations are

$$\begin{aligned} \frac{\partial \mathbf{w}_i}{\partial t} + (\nabla \cdot \mathbf{w}_i + \mathbf{w}_i \cdot \nabla) \mathbf{w}_i + \hat{\mathbf{k}} \times \mathbf{f} \mathbf{w}_i &= -h_i \nabla p_i \\ + (\epsilon_i - \epsilon_{i+1})/\rho + A \nabla^2 \mathbf{w}_i \end{aligned} \quad (1)$$

$$\frac{\partial h_i}{\partial t} + \nabla \cdot \mathbf{w}_i = 0 \quad (2)$$

where $i = 1, 2$ for the two-layer model, $i=1$ for the barotropic and reduced gravity models and

$$\begin{aligned} \nabla &= \frac{\partial}{\partial x} \hat{\mathbf{i}} + \frac{\partial}{\partial y} \hat{\mathbf{j}} & g' &= g(\rho_2 - \rho_1)/\rho \\ p_1 &= gn_1 & f &= f_0 + \beta(y - y_0) \\ p_2 &= p_1 - g'(h_1 - H_1) & \epsilon_i &= \tau_i^x \hat{\mathbf{i}} + \tau_i^y \hat{\mathbf{j}} \\ \mathbf{w}_i &= h_i \mathbf{v}_i = h_i(u_i \hat{\mathbf{i}} + v_i \hat{\mathbf{j}}) \end{aligned} \quad (3)$$

See Appendix A for symbol definitions. In the reduced gravity model the lower layer momentum equation is $g \nabla h = g' \nabla h_1$.

Fig. 2 shows the model domain superimposed on a topographic map of the Gulf of Mexico. The 20° counter-clockwise rotation of the model domain is neglected. The numerical models were driven from rest by prescribed inflow through the Yucatan Straits (southern port) compensated by outflow through the Florida Straits (eastern port). Except at the ports the boundaries are rigid and in almost all cases the no-slip condition is used. \mathbf{w}_i is prescribed at the southern (inflow) port. In most cases a parabolic inflow profile is used for \mathbf{w}_i . Due to the geostrophic tilt in the interface across the port, the velocity maximum is west of the center of the inflow port. At the eastern (outflow) port the normal flow is self-determined using the full x -momentum equation. At inflow points the boundary condition is $u_x = 0$. At outflow points the computational boundary condition is $u_{xx} = 0$. The latter results in upstream differencing for the $(u u)_x$ term, which is lagged in time in this case. The normal pressure gradient is assumed uniform across the port and is determined by an integral constraint requiring the net outflow through the eastern port to

compensate the inflow through the southern port. The tangential velocity component at the ports is usually set at zero 1/2 grid distance outside the physical domain. This weak overspecification eliminates the possibility of outflow at unrealistic angles. Outflow through a channel modeling the Florida Straits is a more realistic approach. This was done in a few cases, but with negligible effect. The semi-implicit numerical models of HT are used in this study. The implicit treatment of the external and internal gravity waves allows much longer time steps in the numerical integration than comparable explicit primitive equation models with a free surface. See HT for further discussion of the numerical models.

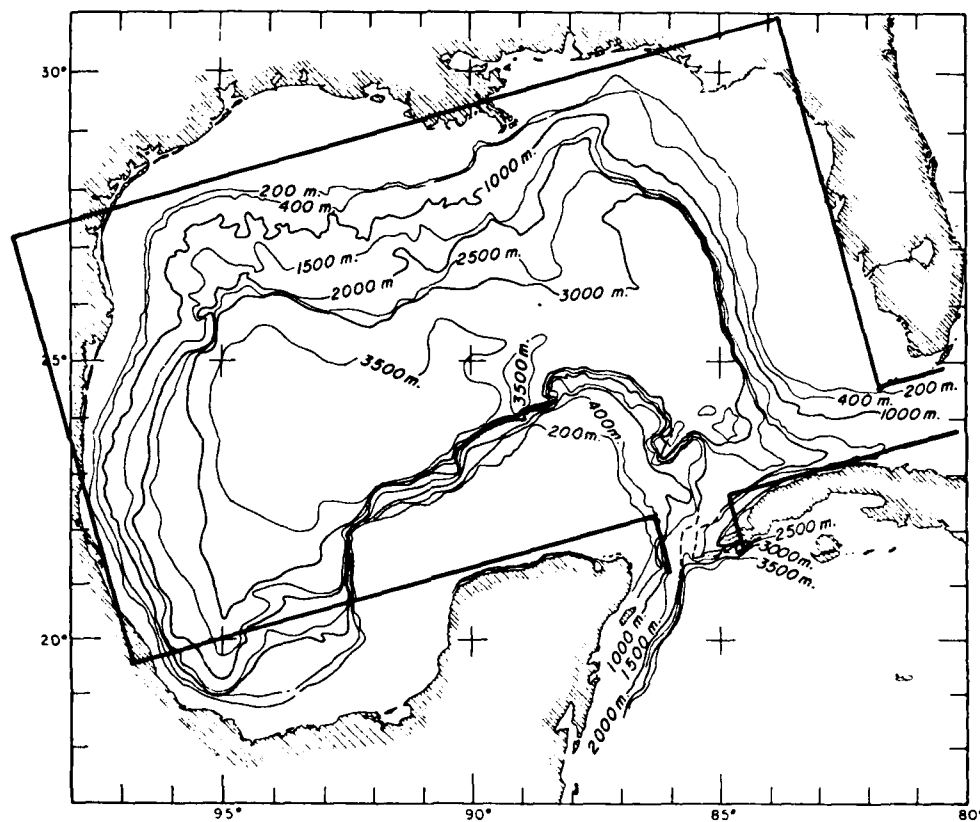


Fig. 2. Bathymetry of the Gulf of Mexico based on U. S. Coast and Geodetic Survey Chart 1007 and soundings on file at the Dept. of Oceanography, Texas A&M University. From Nowlin (1972). The rectangle shows the approximate domain of the numerical model. Inflow and outflow ports are also indicated.

Table 1 presents the parameters of the pivotal experiment for each numerical model. These parameters imply a maximum upper layer inflow velocity of 70-75 cm/s and an internal radius of deformation, $\lambda = (g' h_1)^{1/2}/f \approx 45$ km, about four times less than the observed radius of major eddies shed by the Loop Current. In the two-layer model the value of g' in the table is multiplied

by $(H_1 + H_2)/H_2$ to yield the same internal values for the gravity wave speed as in a reduced gravity model. The inflow transport is spun up with a time constant of 30 days to minimize the excitation of high frequency waves. Potentially important wind driving is neglected to allow focus on the Loop-driven circulation.

TABLE 1
Model parameters for standard case

A	$10^7 \text{ cm}^2 \text{ sec}^{-1}$	β	$2 \times 10^{-13} \text{ cm}^{-1} \text{ sec}^{-1}$
f_0	$5 \times 10^{-5} \text{ sec}^{-1}$	ρ	1 gm cm^{-3}
g	980 cm sec^{-2}	ϵ_i	0
g'	3 cm sec^{-2}	Δx	20 km^*
H_1	200 m	Δy	18.75 km^*
H_2	2800 m	Δt	1.5 hr
Domain Size, x_L by y_L			1600 x 900 km
Southern Port Width, L_{pw}			160 km
Eastern Port Width, L_e			150 km
Center of southern port at x_p			1200 km
Center of eastern port at y_p			75 km
Upper Layer Inflow Transport**			$20 \times 10^6 \text{ m}^3 \text{ sec}^{-1}$ (20 Sv)
Lower Layer Inflow Transport			$10 \times 10^6 \text{ m}^3 \text{ sec}^{-1}$ (10 Sv)
Angle of inflow from x-axis, Θ_I			90°
Inflow spin-up time constant			30 days

For the barotropic model the initial maximum depth is $H=3000$ m and the inflow transport is 30 Sv.

* for a given variable

** also for the standard reduced gravity model

Horizontal friction provides the only dissipation in the models. Because Laplacian friction is a crude parameterization, for convenience $Ah_i \nabla^2 w_i$ was replaced by $A\nabla^2 w_i$ (with minimal effect). The standard eddy viscosity (A) is greater than required for stable integration of the models. HT showed this value yields a constant eddy-shedding period for the Loop Current. Smaller values introduced some irregularity into the period without substantially altering the long-term mean. Although lower eddy viscosities are utilized in some experiments, most employ the larger value to reduce the length of the integration required to obtain stable statistics, and to facilitate the analysis of the results. Fig. 3 shows the idealized Gulf of Mexico

topography used in some of the numerical experiments. Typically the models were integrated five years to statistical equilibrium.

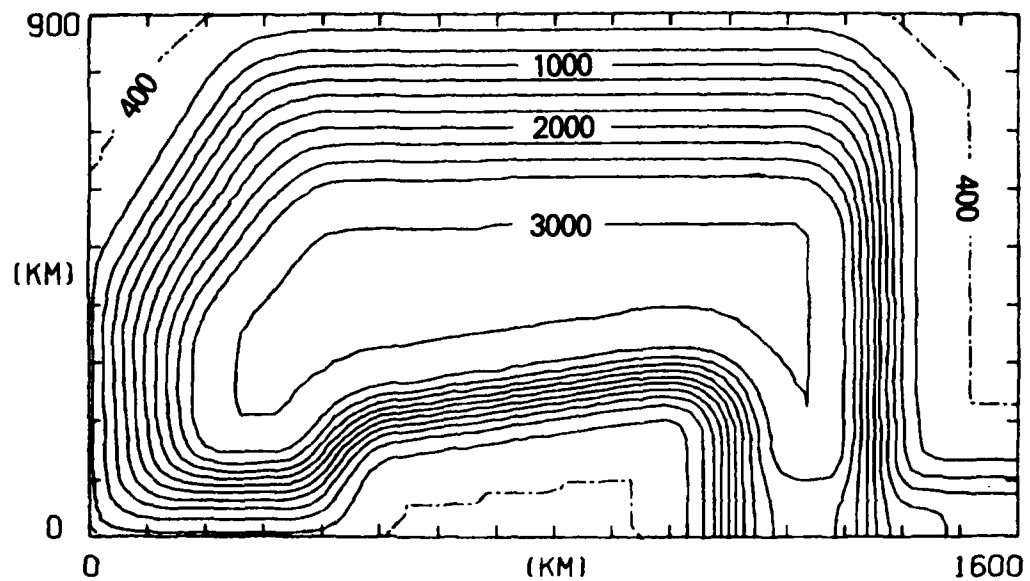


Fig. 3. Bathymetry of the idealized Gulf of Mexico model. The deepest water is at 3000 m and the shallowest topography is 400 m deep. The contour interval is 250 m. (From HT).

3. AN ATTEMPT TO SIMULATE THE EDDY SHEDDING BY THE LOOP CURRENT

Our first goal was to determine which, if any, of the models could demonstrate eddy shedding with a realistic eddy diameter, amplitude, shedding period, and propagation. Within the framework of the two-layer model, the first simulation was made as realistic as possible including the idealized topography shown in Fig. 3. A longstanding hypothesis (Cochrane, 1965) maintains that the Loop Current exhibits an annual eddy shedding cycle due to seasonal variations in the flow through the Yucatan Straits which affect the penetration distance of the Loop Current. When the Loop retreats, eddy shedding is presumed to occur. Despite this hypothesis, the model was first driven by a steady inflow to see if the Loop Current would shed eddies due to purely internal mechanisms. This might then establish a natural frequency for the eddy shedding.

The first experiment utilizes the parameters of Table 1 and the topography of Fig. 3 except that the upper layer inflow transport is 25 Sv, the lower layer 5 Sv. Fig. 4 illustrates an eddy shedding cycle from this experiment using a sequence of four synoptic maps of the pycnocline anomaly (PA). The PA is the

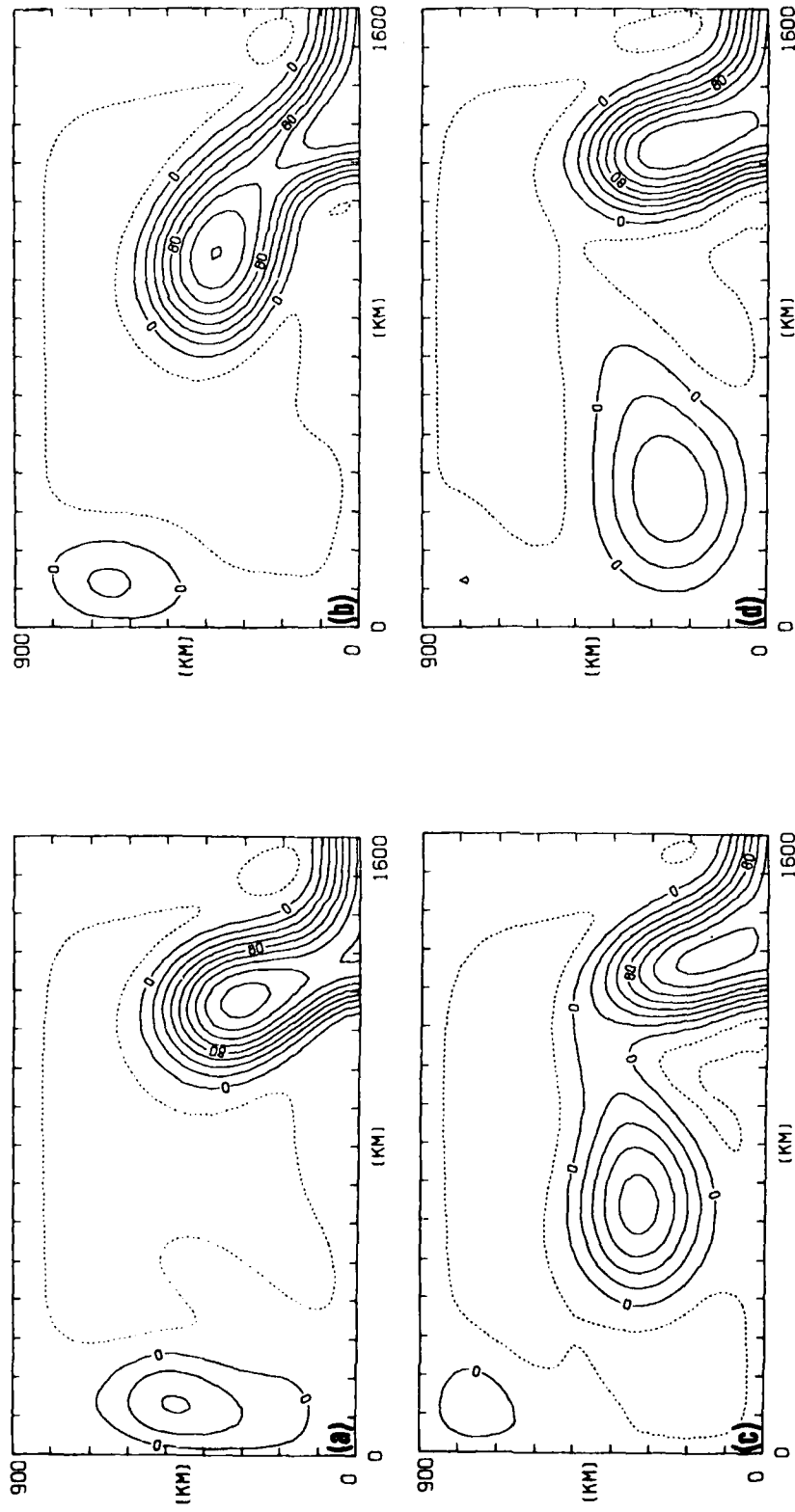


Fig. 4. Sequence of synoptic maps of PA at 70-day intervals showing the life cycle of an eddy starting at day 2210. The contour interval is 20 m. In all the figures dashed contours are negative. PA is positive downward. The case shown here uses the parameters of Table 1 and the topography of Fig. 3 except that the upper layer inflow transport is 25 Sv, the lower layer 5 Sv. (From HT).

deviation of the interface between the layers from its initial flat elevation and is positive downward (upper layer thickness greater than initial). Fig. 4a shows the Loop Current has penetrated into the Gulf and is beginning to form an anticyclonic eddy. In Fig. 4b the Loop Current has bent westward and an eddy is about to break off. Fig. 4c shows the Loop Current and an eddy just after an eddy-shedding event. In Fig. 4d the eddy has drifted westward while the Loop Current has penetrated further into the Gulf. Fig. 4a, b shows that when an eddy reaches the western boundary, it drifts northward with final decay in the northwest corner of the basin.

The cycle of Loop Current penetration into the Gulf, westward bending and eddy shedding is repeated with a period of about 290 days, close to the quasi-annual period observed. Contrary to the popular hypothesis, time variations of the inflow are not required for the model Loop Current to exhibit realistic quasi-annual eddy shedding, a striking result first noted by HT. The model also predicts a realistic eddy diameter, amplitude, and westward propagation speed. In subsequent experiments HT found that realistic time variations in the upper layer inflow can have a significant influence on the eddy shedding. However, the eddy shedding is dominated by the natural period, not the period of the forcing, a topic we shall not pursue here. In Section 7 we do examine an important effect of topography and lower layer inflow through the Yucatan Straits on the eddy shedding.

4. A SIMPLE TEST FOR THE INSTABILITY MECHANISM

The remaining sections are designed to provide some insight into the dynamics of the Loop Current-eddy system. We might be tempted to undertake a stability analysis to find instability mechanisms, unstable wavelengths, and growth rates, but we would anticipate that the configuration of the current would be troublesome. However, there are more fruitful approaches than this. Nevertheless, we will start with one simple test for the primary instability mechanism by using the reduced gravity model. If it produces results similar to the two-layer model, then we have eliminated baroclinic instability as an essential element of the dynamics, and the primary instability mechanism is a horizontal shear instability of the internal mode, a barotropic instability.

Fig. 5 compares (a) the experiment with topography discussed in Section 3, (b) a two-layer flat-bottom experiment using the standard parameters from Table 1, and (c) a reduced gravity experiment using appropriate parameters from Table 1. Shown is a latitude vs. time (y vs. t) plot of PA at a longitude 190 km west of the center of the southern port. In all three cases the PA shows a regular progression of discrete eddies with similar eddy diameter, amplitude, and shedding period. However, the experiment with topography (Fig. 5a) did not begin to shed eddies for almost three years, a point addressed in Section 7. With standard parameters the barotropic model evolved to a steady state without shedding eddies, a matter discussed in Section 6.

The results shown in Fig. 5 lead us to conclude that a horizontal shear instability of the internal mode is dominant. The two-layer model with Fig. 3 topography, the two-layer flat-bottom model, and the reduced gravity model do not agree in all the parameter space we explored (see Section 8), but they do agree for a regime in accord with observed features of the Loop Current-eddy system. Since the reduced gravity model is the simplest of the models to provide a realistic simulation, it is used in much of our analysis. The question of barotropic vs. baroclinic instability is addressed further in Section 8 using eddy-mean energetics and other signatures of the instability mechanisms.

5. CAV TRAJECTORIES AND ROSSBY WAVE THEORY ELUCIDATE THE LOOP CURRENT - EDDY SHEDDING DYNAMICS

Constant absolute vorticity (CAV) trajectories and Rossby wave theory are useful aids in understanding the dynamics of the Loop Current and the eddy shedding including the penetration of the Loop Current into the Gulf and the eddy diameter, shedding period, and westward propagation.

5.1 CAV trajectory analysis

CAV trajectories are based on conservation of potential vorticity on a β -plane and on steady, frictionless, geostrophically balanced flow. In the reduced gravity model this implies that contours of upper layer depth are streamlines, and thus absolute vorticity is also conserved. The CAV

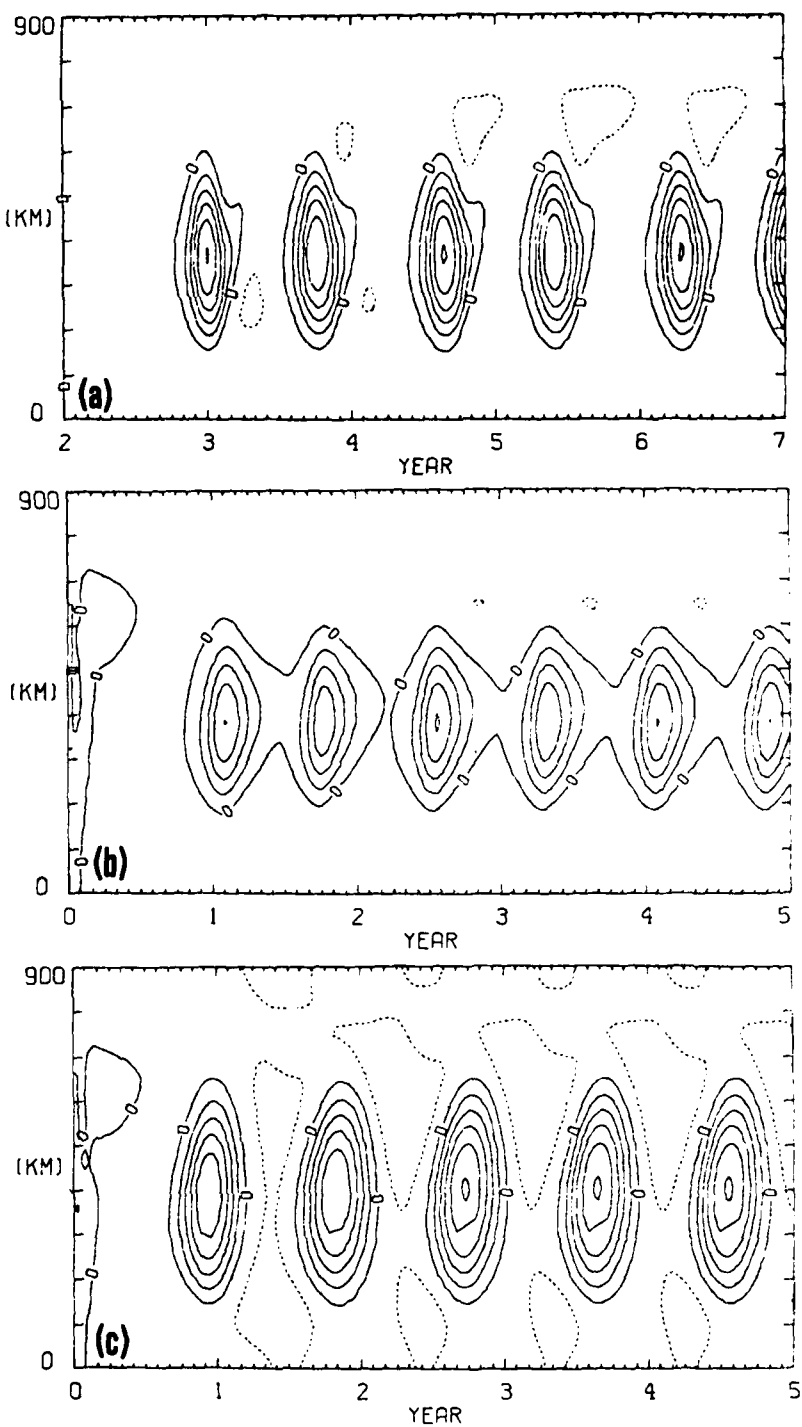


Fig. 5. Time variations of PA 190 km west of the center of the inflow port for three cases: (a) case shown in Fig. 4 which includes topography, (b) standard two-layer flat-bottom case using parameters from Table 1, and (c) standard reduced gravity case using appropriate parameters from Table 1. A regular progression of eddies through the north-south cross section is shown in each case. The contour interval is 30 m. (From HT).

trajectories are calculated from

$$\sin\theta \frac{d\theta}{dy} = -\frac{\beta}{v_c} y + \frac{v_{co}}{v_c r_0} \quad (4)$$

where θ is the angle of the current with respect to the positive x -axis, v_c is the velocity at the core of the current, r_0 is the radius of curvature, and the subscript, 0, indicates a value at the origin of the trajectory calculation (e.g., see HT; Reid, 1972; Haltiner and Martin, 1957).

Fig. 6 shows CAV trajectories superimposed on the model domain for $v_c = 75$ cm/s, $r_0 = \infty$ and six different values of θ_0 . Since $r_0 = \infty$, the origin is the first inflection point after inflow (see Fig. 4), and not the inflow port as implied by the figure. As θ_0 increases, the trajectory increasingly tends to loop back on itself. When $\theta_0 = 130^\circ$, the CAV trajectory intersects itself at the origin, a physically impossible situation for a steady flow. Thus, when θ_0 becomes large some physical instability of the Loop Current can be anticipated.

In Fig. 6 θ_0 is varied to simulate the formation of an eddy, but it really represents a sequence of steady state solutions to (4). Although the eddy-shedding Loop Current is not steady, its evolution is sufficiently slow to consider it in isostatic adjustment with respect to CAV trajectories. In the time a fluid particle in the Loop moves from the west side to the east side, the Loop bends westward only 5 to 10% of the Loop diameter.

5.2 Influence of Rossby waves

How does the model Loop Current bend westward when the angle of inflow through the Yucatan Straits is not varied? We can gain some insight into this by examining the continuity equation, (2). If the mass divergence is geostrophic, it will propagate westward as a nondispersive internal Rossby wave. (Note the converse is not true near the equator). For geostrophic divergence (2) becomes

$$\frac{\partial h_1}{\partial t} - \beta V_g/f = \frac{\partial h_1}{\partial t} - c_{ir} \frac{\partial h_1}{\partial x} = 0 \quad (5)$$

where V_g is the geostrophic meridional transport and

$$c_{ir} = \beta g' h_1 / f^2 = \beta \lambda^2 \quad (6)$$

is the nondispersive internal Rossby wave speed.

The importance of nondispersive Rossby wave propagation can be anticipated from appropriate isolated vortex theory (McWilliams and Flierl, 1979), because 1) $r/\lambda \approx 4$ where r is the eddy radius and λ is the internal radius of deformation, and 2) the beta Rossby number, $R_B = v_c / (\beta r^2) \approx 1$ for the eddies. From the linear

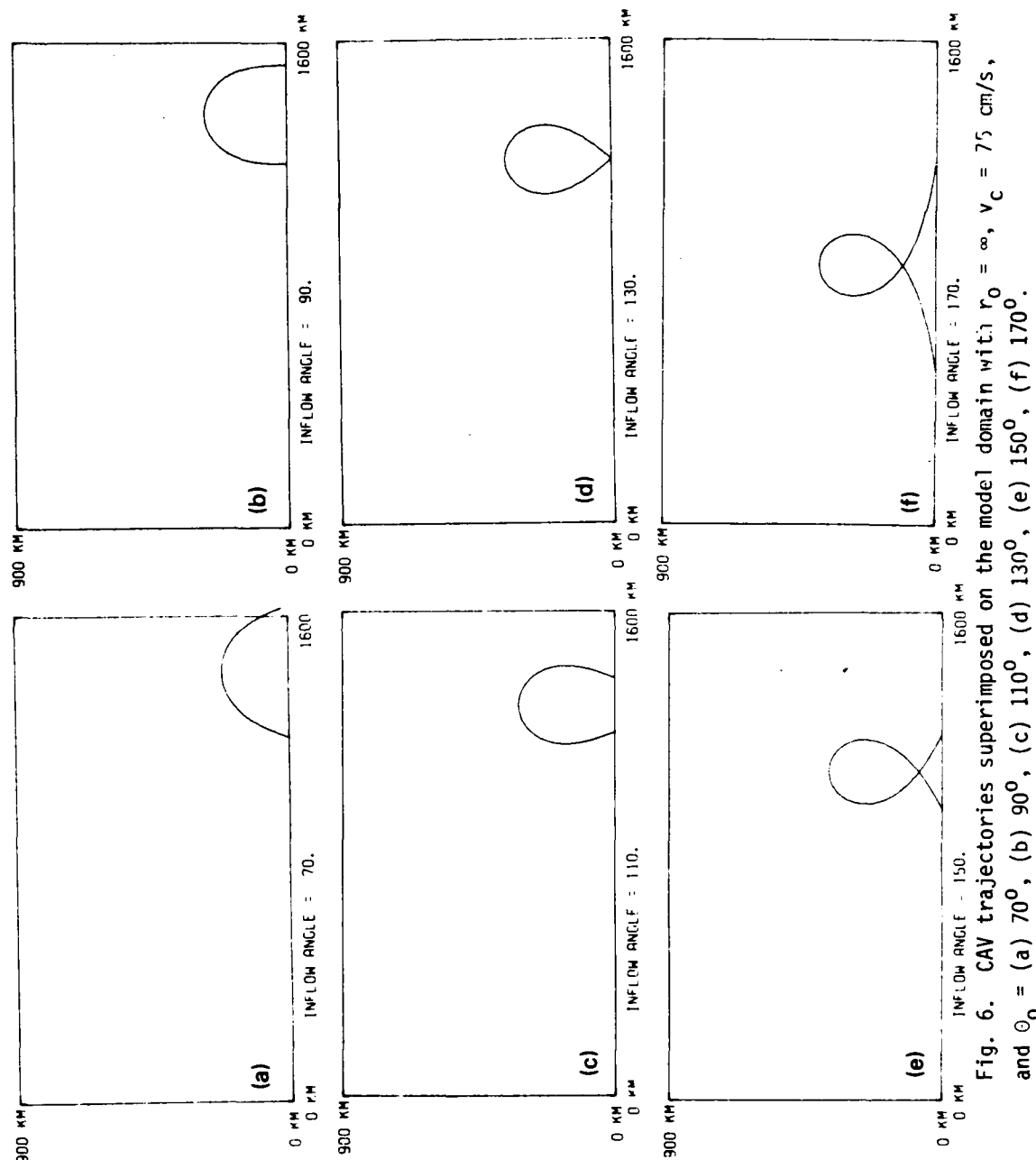


Fig. 6. CAV trajectories superimposed on the model domain with $r_0 = \infty$, $v_c = 75 \text{ cm/s}$, and $\theta_0 =$ (a) 70° , (b) 90° , (c) 90° , (d) 110° , (e) 130° , (f) 170° .

phase speed for Rossby waves

$$c_r = \beta / (k^2 + \ell^2 + \lambda^{-2}) \quad (7)$$

where k and ℓ are zonal and meridional wavenumbers, respectively, the dispersive and nondispersive contributions are equal for circular eddies when $r/\lambda = \pi/\sqrt{2} = 2.22$. Hence, we also expect a significant but secondary contribution from dispersive Rossby wave propagation.

Fig. 7 compares the instantaneous mass divergence ($\nabla \cdot \mathbf{V}_1$) and the geostrophic mass divergence ($-\text{curl} \frac{\partial h_1}{\partial x}$) for the standard reduced gravity experiment at two different stages in the eddy shedding cycle. The usefulness of the instantaneous mass divergence fields must be questioned, since they are easily dominated by rapid oscillations and computational noise. The absence of these contaminations was verified by showing that the instantaneous mass divergence and the 20-day mean are virtually identical. From (2) the 20-day mean can be determined from the change in h_1 in 20 days.

Near the ports and near the western boundary the mass divergence is far from geostrophic. Note particularly in Fig. 7e the ageostrophic mass convergence in the southeastern part of the basin associated with the northward penetration of the Loop Current. Also note that mass convergence occurs at the center of the eddy during its formation (an anticyclonic inflow), while mass divergence occurs at the center (anticyclonic outflow) after the eddy separates from the Loop and slowly decays. However, in the westward bending Loop and in the recently shed eddy the total mass divergence and the geostrophic mass divergence are quite similar. This clearly demonstrates an important contribution of non-dispersive internal Rossby wave propagation to the westward bending of the Loop Current and the westward propagation of the eddies. Other contributions such as nonlinear and dispersive Rossby wave propagation are not accounted for here. Still, we have identified an important mechanism which acts to bend the Loop Current westward. Thus, it also produces a counter-clockwise rotation of the current at the first inflection point after inflow (see Fig. 4). This in turn produces changes in the CAV trajectory (Fig. 6) which leads us to anticipate the formation and shedding of an eddy.

5.3 Two time scales associated with the eddy shedding

Note that westward bending of the current and the tendency for it to loop back on itself can be understood without invoking an instability mechanism. An instability mechanism appears essential only to explain the separation of the eddy from the Loop. Thus, two time scales are associated with the eddy shedding period: 1) the long time scale for the Loop Current to penetrate into the Gulf and bend westward into an unstable configuration, and 2) the much shorter time scale for the growth of the instability as the eddy separates from

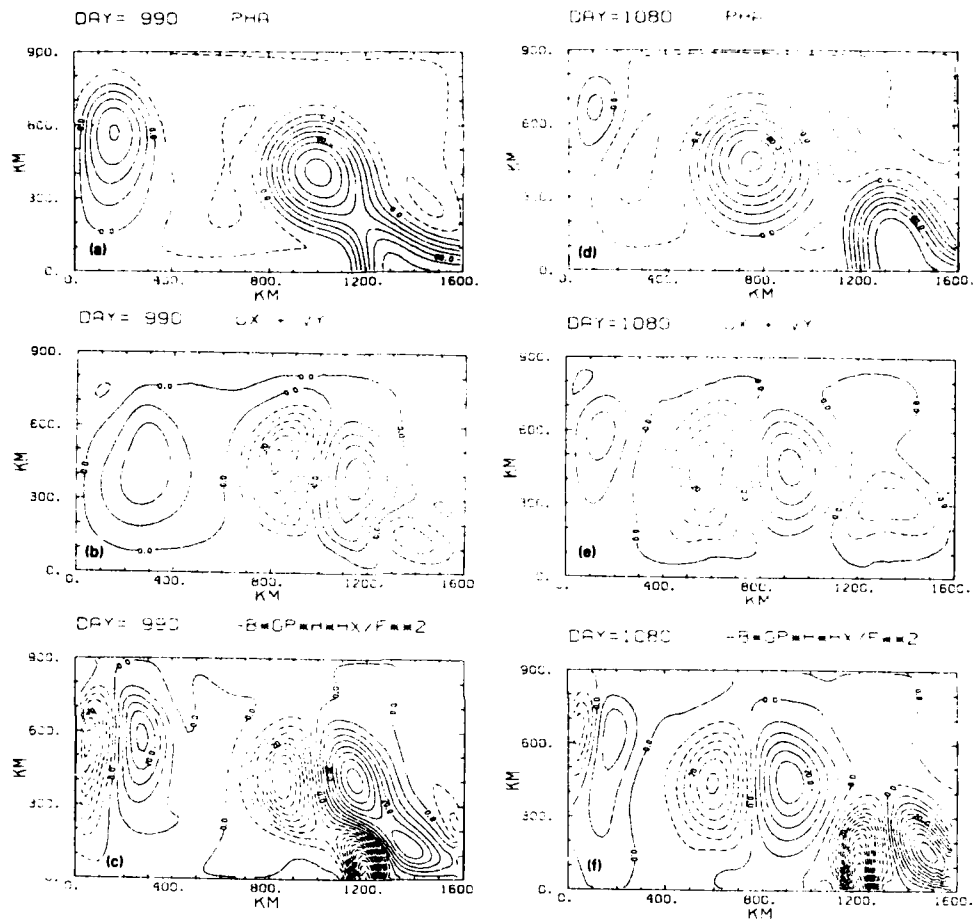


Fig. 7. Shows (a,d) the PA for the standard reduced gravity experiment, which uses the pertinent parameters from Table 1, and compares the associated (b,e) instantaneous mass divergence ($\nabla \cdot \mathbf{V}_1$) and (c,f) geostrophic mass divergence ($-\mathbf{c}_{ir} \frac{\partial h}{\partial x}$). Two different stages of an eddy cycle are illustrated at days 990 (left) and 1080 (right). The contour intervals are 20 m for PA and 10^{-4} cm/s for mass divergence.

the Loop Current. This suggests a repeated spin-up of the Loop Current which eventually becomes unstable. Although it may, it is not clear that the Loop Current must satisfy any criterion for instability during much of the eddy cycle.

5.4 Hypothesis testing

The CAV trajectory analysis, Rossby wave theory, and the vorticity equation can be used to formulate a number of quantitative hypotheses concerning the northward penetration of the Loop Current into the Gulf, the latitude at which the westward bending occurs, and the eddy diameter, shedding period, and westward propagation. We will formulate the appropriate scales and then test them as hypotheses for the dynamics governing the Loop Current-eddy system predicted by the reduced gravity numerical model. The vorticity equation for the reduced gravity model is

$$\frac{\partial \zeta_1}{\partial t} + \mathbf{v}_1 \cdot \nabla \zeta_1 + (f + \zeta_1) \left(\frac{\partial u_1}{\partial x} + \frac{\partial v_1}{\partial y} \right) + \beta v_1 = A \nabla^2 \zeta_1 \quad (8)$$

where $\zeta = v_x - u_y$ is the relative vorticity.

5.5 Eddy diameter, Loop Current penetration, and latitude of westward bending.

The beta Rossby number, R_B , is the ratio of relative to planetary vorticity advection, and $R_B=1$ provides a minimum inertial length scale, $L_{BI} = (v_c/\beta)^{1/2}$, over which β is important. We hypothesize that this determines the latitude at which the Loop Current bends westward. The frictional length scale over which β is important, $L_{BF} = (A/\beta)^{1/3}$, is much smaller. $L_{BI} = 191$ km and $L_{BF} = 37$ km for our standard reduced gravity experiment. This implies that inertia will prevent Rossby wave action from bending the Loop Current westward at a higher latitude than friction.

We also find that $R_B=1$ and $r = (v_c/\beta)^{1/2}$ are appropriate values for the radius of the eddies formed by the Loop Current. However, without further analysis it is not clear why the eddies from the Loop Current select this scale. McWilliams and Flierl (1979) have studied persistent isolated eddies with $R_B \gg 1$ and note that typically $R_B > 1$ for Gulf Stream rings.

For insight into the scale selection by the Loop Current eddies, we turn to the CAV trajectory analysis and present a discussion similar to HT. Integration of (4) assuming $v_c = \text{constant}$ along a streamline at the core of the current yields

$$\cos \theta = \cos \theta_0 + \frac{\beta}{2v_c} y^2 - y/r_0 \quad (9)$$

This neglects the point that $v_c \neq \text{constant}$ along a streamline, if there are variations in radius of curvature. The north-south diameter of an eddy between

speed maxima can be estimated by setting $\theta_0 = \pi$ at the southernmost extent (the origin) and $\theta = 0$ at the northernmost extent. Then for $r_0 = \infty$, (9) becomes

$$d = 2r = 2(v_c/\beta)^{1/2} \quad (10)$$

where d is the desired diameter, a north-south "dimension" for "stationary planetary eddies" noted by Rossby (1940, p. 82). This implies that $R_B = v_c/(\beta r^2) = 1$ for the Loop Current eddies.

The northernmost penetration of the core of the current, b , from the latitude of θ_0 can be estimated from (9) by setting $\theta = 0$ at the northernmost extent. This yields

$$b = \left[\frac{r^2}{r_0} + \frac{r^4}{r_0^2} + 2r^2(1-\cos\theta_0) \right]^{1/2} \quad (11)$$

For $r_0 = \infty$, (11) reduces to

$$b = d \sin^{1/2}\theta_0 \quad (12)$$

Thus, with $r_0 = \infty$ the maximum amplitude for a CAV trajectory occurs when $\theta_0 \rightarrow \pi$. This is what (10) really represents, since in this case the CAV trajectory loops back on itself northwest of the origin (see Fig. 6). For $\theta_0 = 130^\circ$ the CAV trajectory loops back on itself at the origin in a figure 8 (Fig. 6d) and $\sin^{1/2}\theta_0 \approx .9$. We might anticipate that the horizontal shear instability would occur when the first inflection point of the current after inflow rotates counterclockwise to $\sim 130^\circ$. In the numerical solutions where the flow is not steady, potential vorticity is not perfectly conserved, and other conditions of the CAV analysis are not perfectly met, we find that eddy separation occurs when this angle is somewhat $> 130^\circ$ (see Fig. 4). In this case a CAV trajectory would loop back on itself northwest of the first inflection point after inflow. However, a col is configured such that eddy separation actually occurs southeast of this inflection point. From the standpoint of estimating the amplitude of the CAV trajectory (with $r_0 = \infty$) and thus the eddy diameter, the value of θ_0 when the eddy separates from the Loop Current is not critical, since $\sin^{1/2}\theta_0$ varies only 10% from $\theta_0 = 130^\circ$ to $\theta_0 = \pi$.

5.6 Tests of some dynamical hypotheses

Tests of some hypotheses concerning the dynamical behavior of the Loop Current are summarized in Table 2. Immediately apparent is the pervasive role of differential rotation β . The results are based on 35 reduced gravity experiments (34 for $L_{\beta I}$ and L_{np}) from Table 2 of HT, the same ones they used in similar hypothesis testing.

TABLE 2

Tests of some dynamical hypotheses for the Loop Current-eddy system.

	% bias	correlation	numerical	Standard reduced gravity case theoretical
1. Eddy radius				
$r = (v_c/\beta)^{1/2}$	6	.87	186 km	191 km
2. Distance from the southern boundary to the latitude of westward bending by the Loop Current.				
$L_{\beta I} = (v_c/\beta)^{1/2} = r$	-7	.75	201 km	186 km
	-1	.77	201 km	191 km
3. Maximum northward penetration of the Loop Current.				
$L_{np} = L_{\beta I} + b = 3r$	-2	.99	574 km	560 km
	4	.89	574 km	573 km
4. Westward propagation speed of the eddies.				
$c_{ir} = \beta \lambda^2 = \beta g' h_1 / f^2$	40	.99	3.21 cm/s	4.57 cm/s
$c_r = \beta / (k^2 + \ell^2 + \lambda^{-2})$	-2	.97	3.21 cm/s	3.49 cm/s
5. Eddy shedding period.				
$p_e = A_0 + A_1 r (1 + \cos \theta_I)^{1/2} / c_e$	-	.95	327 days	359 days
	-	.96	327 days	338 days

The % bias and the linear correlation are statistics for the theoretical prediction vs. the values observed in the reduced gravity numerical model. They are based on 34 to 35 numerical experiments from Table 2 of HT, the same ones they used in their hypothesis testing for similar quantities. The % bias $\equiv ((m_0 - m_p)/m_0)$ where m_0 and m_p are the means of the observed and predicted values, respectively. The two rightmost columns present the results observed and predicted for the standard reduced gravity experiment which uses the pertinent parameters from Table 1. Results from two tests are presented for $L_{\beta I}$, L_{np} and p_e . On the upper line values of r and c_e observed in the numerical model were used in the predictor. On the lower line the theoretical values were used for r and c_e (i.e. c_r for c_e).

In estimating r , $L_{\beta I}$, and L_{np} the maximum speed at inflow was used for v_c . One-half the north-south diameter between speed maxima was used for the eddy radius from the reduced gravity numerical model. The distance from the southern boundary to the southern end of the eddy diameter was used for $L_{\beta I}$ and from the southern boundary to the northern end of the diameter for L_{np} . These were measured as the eddy center passed a longitude 110 km west of the western boundary of the inflow port. This was also close to the inflection point which

exhibited a large angle at this time (see Figs. 4 & 7). Thus, the theoretical estimate of b was simplified by setting $\theta_0=\pi$ and $r_0=\infty$. This yields $b=2r$.

The agreement between the theoretical estimates of r , L_{BI} , and L_p and the values calculated from the numerical model is remarkably good. In most cases the agreement for r was within 5%. However, at low Reynolds numbers and low latitudes, (10) overestimated the model value by > 10%. In the experiments with low Reynolds numbers downstream attenuation of the current appears to explain this. At low latitudes the assumption of isostatic adjustment with respect to CAV trajectories is not as good due to an increased westward propagation speed. Also r/λ is less, so the Loop and the eddies are more subject to dispersion. In estimating L_{BI} and L_{np} , values of r from the numerical model were used for the upper line and theoretical values for the lower line.

In estimating λ , h_e from Table 2 of HT was used for h_1 and the value of f at the latitude of the eddy center was used. The correlation between c_{ir} and the westward propagation speed of shed eddies is extremely high, but the theoretical speed is 40% greater than observed in the reduced gravity numerical model. When the dispersive contribution is included, the mean Rossby wave speed and the mean observed westward propagation speed differ by < 2%. The value of $k^2+\ell^2$ was estimated by assuming circular eddies and using the theoretical values for r .

In Table 2 a regression equation is used to test the hypothesis that the eddy shedding period is a multiple of the time required for an eddy to move one eddy radius westward. The multiple depends on the angle of inflow for the current, θ_I . The upper line presents the results when values measured from the numerical model are used for r and c_e (the westward propagation speed). On the lower line theoretical values (c_r and c_e and (10) for r) are used. The regression coefficients are $A_0=45.1$ days and $A_1=4.67$ for the upper line and $A_0=-.2$ days and $A_1=5.34$ for the lower line. The regression coefficient, λA_1 , is a kind of inverse Strouhal number (nondimensional period) if we take the eddy diameter, d , as the appropriate diameter, and the westward propagation speed of the eddies (rather than the injection velocity) as the appropriate velocity. The Strouhal numbers ($S=2/A_1$) implied by the two regression results are .43 for the upper line and .37 for the lower line. If d was the half-wavelength for a continuous wavetrain, then the Strouhal number would be $S=.5$.

The eddy shedding period also exhibits a weak dependence on the eddy viscosity A , primarily because this affects the amount of entrainment or detrainment downstream. The result is an eddy-shedding period which increases with increasing Reynolds number, $Re=v_{ci}L/A$ where v_{ci} is the maximum velocity at inflow and L is half the inflow (southern) port width. At high Reynolds numbers, secondary circulations of the Loop-eddy system become significant and introduce some irregularity into the eddy shedding period.

6. REGIMES FOR THE LOOP CURRENT IN THE REDUCED GRAVITY MODEL

6.1 The eddy-shedding regime (E)

The preceding section examined some of the dynamics of the eddy shedding by the Loop Current and demonstrated the usefulness of CAV trajectory analysis and Rossby waves in explaining the behavior. It also demonstrated the important role of differential rotation (β) in most aspects of the eddy-shedding dynamics. We will call the eddy-shedding regime the E regime.

6.2 The steady westward spreading regime (W)

This section investigates the existence of other flow regimes in the neighboring parameter space. One such regime was found by reducing the Reynolds number, $R_e = v_c L/A$, where L is the half-width of the port. This acts both to damp physical instabilities in the current and to decrease potential vorticity conservation, thus reducing the tendency of the current to loop back on itself. The result is a steady solution with a westward bending Loop Current as shown in Fig. 8a. We will call this the W regime. Fig. 8a was obtained by increasing the eddy viscosity (A) from 10^7 to $3 \times 10^7 \text{ cm}^2/\text{s}$ in the standard reduced gravity model. Steady linear viscous solutions (where $\beta v_1 = A \nabla^2 \zeta_1$) and weakly nonlinear solutions belong to the W regime. As mentioned in Section 5, the latitude of westward bending after inflow is determined by the larger of $L_{\beta I}$ and $L_{\beta F}$. As noted by HT, the mean of the standard reduced gravity experiment over an eddy cycle is very similar to Fig. 8a. This implies that in the mean the eddies drive a northward-flowing western boundary current.

Between the E and W regimes there is a transition regime (T) with eddies superimposed on a westward bending Loop Current. This is illustrated in Fig. 8b using the standard reduced gravity model except that $A = 2.5 \times 10^7 \text{ cm}^2/\text{s}$. Experiments that exhibited both eddy shedding and an unbroken, westward bending zero contour (like Fig. 8b) were assigned to the T regime.

6.3 Steady source-sink regime (N)

A third major regime we call the N regime is found by increasing the beta Rossby number, $R_B = v_c / (\beta L_p^2)$, where L_p is half the distance separating the centers of the inflow and outflow ports. The N regime occurs when $R_B \geq 2$. At sufficiently low Reynolds numbers the transition between the N and W regimes is determined by the beta Ekman number, $E_B = A / (\beta L_p^3)$, as discussed in the next subsection. In either case the N regime is characterized by a steady source-sink flow with no westward bending by the Loop Current. It is illustrated in Fig. 9 by two variations on the standard reduced gravity experiment. In Fig. 9a $\beta = 0$ and $R_B = \infty$. Note that $\beta > 0$ is essential for the westward bending of the Loop Current and the eddy shedding shown in Figs. 4 and 7. With R_e sufficiently high, we would expect some instability to occur in the source-sink current, but not the quasi-annual eddy shedding exhibited by the Loop Current.

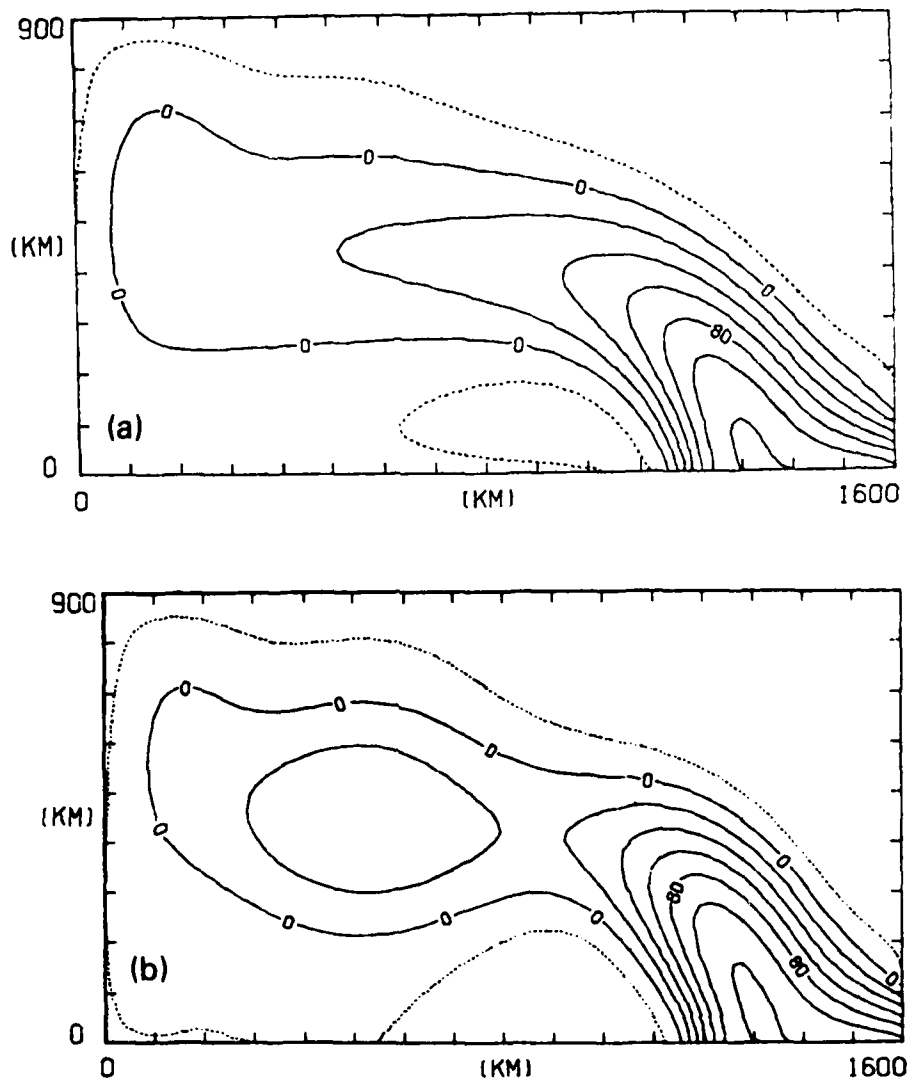


Fig. 8. Illustration of (a) steady regime W and (b) time-dependent regime T. The standard parameters for the reduced gravity model were used except that in (a) $A = 3 \times 10^7 \text{ cm}^2/\text{sec}$ and in (b) $A = 2.5 \times 10^7 \text{ cm}^2/\text{s}$. The contour interval is 20 m. In regime W the Loop Current bends westward and is steady. In regime T steady shedding is superimposed on a westward bending loop instead of being discrete as in Fig. 7a, d.

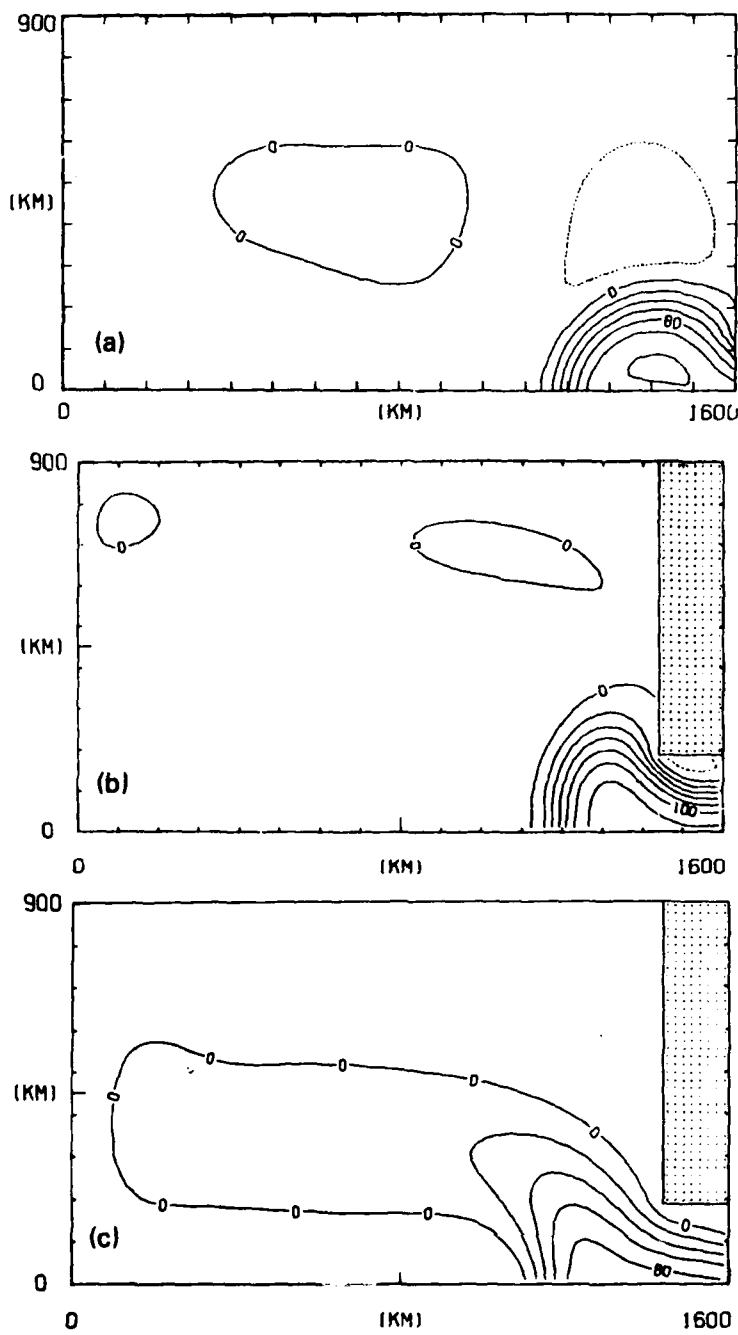


Fig. 9. Illustration of the steady regime N for the standard reduced gravity experiment except that $\beta = 0$ and (b) a section of land was added to approximate the west Florida shelf. Steady mixed regime M is shown in (c) with parameters chosen to approximate those of Mellor and Blumberg (1981), including $Re = 10.8$ and $R_B = 1.19$.

In a second experiment the port separation was reduced by inserting a land mass which approximates the location of the West Florida Shelf (Fig. 9b). In this case L_p was measured using a port centered 75 km south of the western boundary of the inserted land mass. From Section 5 $r=L_{BI}=(v_c/\beta)^{1/2}$, thus the beta Rossby number can also be expressed as $R_B=(r/L_p)^2$ or $R_B=(L_{BI}/L_p)^2$. Since the N regime occurs for $R_B > 2$, this implies a critical port separation $2L_p = \sqrt{2}r = \sqrt{2}L_{BI}$. From the definition of R_B , both β and L_p play a similar role in determining the N regime. Otherwise, their roles are not similar. As long as R_B is small enough for eddy shedding to occur, the E regime is quite insensitive to L_p , but most aspects of the dynamics are very sensitive to β .

The N regime occurs when the Loop Current reaches a steady state before penetrating far enough into the Gulf to bend westward. From (12) and Fig. 6d a CAV trajectory with $r_0=\infty$ can penetrate into the Gulf with no westward bending a distance $b = \sqrt{2}r = \sqrt{2}L_{BI}$ (the same as the critical port separation). Using this as an estimate of the maximum possible Loop Current penetration in the N regime is consistent with our present numerical results (see HT for further discussion).

The transition between regimes N and E is quite abrupt and a transition regime has not been found in any of our numerical experiments. The transition between regimes N and W is broader. In this mixed regime (M) the westward spreading of the Loop Current is significantly less than it would be if the port separation were infinite. The numerical simulation of the Loop Current by Blumberg and Mellor (1981) belongs to this M regime. Fig. 9c shows a reduced gravity analog of that experiment using our estimates of appropriate parameters, including $Re=10.8$ and $R_B=1.19$ (See Appendix B for other parameters used). Considering our neglect of the 20° counterclockwise rotation of the basin, our pattern for the Loop Current is remarkably similar to that from the much more complicated and expensive model of Blumberg and Mellor (1981). Experiments were assigned to the M regime if the central contour on inflow exhibited any westward bending, but the amplitude of the Loop PA was $< 30\%$ of the maximum a distance $(v_{ci}/\beta)^{1/2}$ west of the center of the inflow, where v_{ci} is the maximum velocity at inflow.

6.4 Stability regime diagram

Three nondimensional parameters from the vorticity equation (Eq. (8)) play an important role in determining the stability regimes for the Loop Current in the reduced gravity and flat-bottom barotropic models. They are the Reynolds number (Re), the beta Rossby number (R_B), and the beta Ekman number (E_B). Only two of these are independent. Provided the same scales are used, $E_B=R_B/Re$. Fig. 10 shows the parameter space occupied by the various regimes on a stability diagram of Re vs. R_B . Eddy shedding occurs for $R_B \leq 2$ and $Re \geq 25$ for the reduced

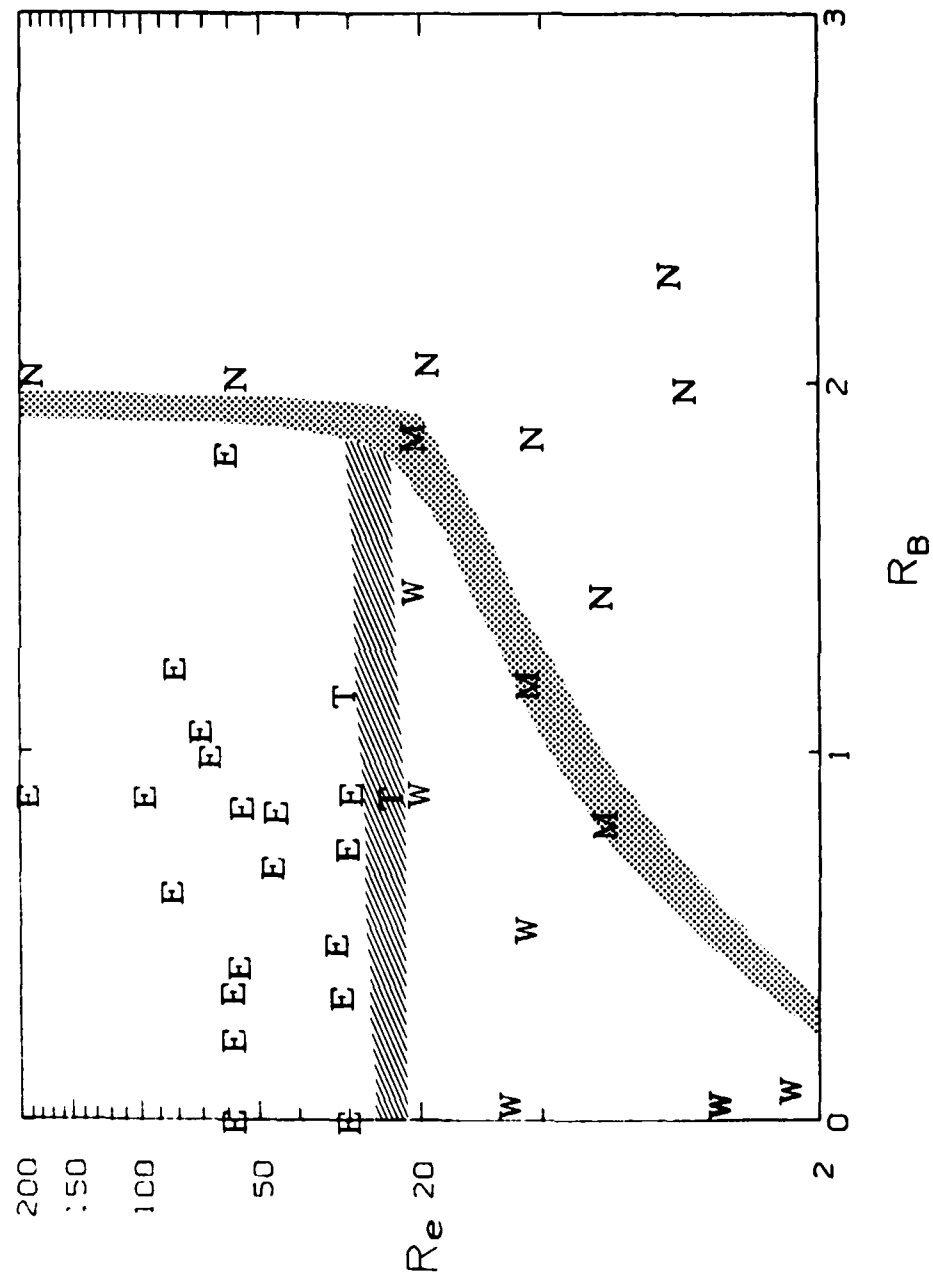


Fig. 10. Regime diagram for three stability regimes and transition regimes between them for a reduced gravity model of the Gulf of Mexico. The axes are the Reynolds number (Re) and the beta Rossby number (R_B). The regimes are (E) eddy shedding (Figs. 5c and 7a, d), (W) steady westward spreading (Fig. 8a), (N) steady source-sink (Fig. 9a, b), (T) transition between E and W with eddy shedding superimposed on a mean loop (Fig. 8b) and (M) transition between steady regimes N and W (Fig. 9c).

gravity model, $Re \geq 40$ for the flat-bottom barotropic model (not shown). Apparently, the dispersive nature of Rossby waves in the barotropic model is a catalyst which leads to a higher critical Reynolds number (Re_C). The transfer of energy to the lower layer in the two-layer models seems to have a similar effect on Re_C .

At low Reynolds number the transition between regimes N and W depends upon $E_B = R_B L / (Re L_p)$. The correction factor L/L_p is required because we have not used L_p in our definition of Re . This transition is clearly defined on our stability diagram only if L/L_p is fixed. From Section 5.5 R_B and E_B can be expressed in terms of the latitude of westward bending by the Loop Current, i.e. $R_B = (L_{\beta I} / L_p)^2$ and $E_B = (L_{\beta F} / L_p)^3$. Whether R_B or E_B determines the transition to the N regime depends upon the relative importance of $L_{\beta F}$, the frictional length scale, and $L_{\beta I}$, the inertial length scale, in determining the latitude of westward bending by the Loop Current. From the regime diagram, the transition between these two criteria occurs when $2.5 L_{\beta F} \approx L_{\beta I} / \sqrt{2}$.

Other parameters not accounted for here such as inflow angle, basin geometry, and basin orientation may also have some influence on the regime selection. Additional influences in the two-active-layer model are discussed in the next two sections.

7. PREVENTION OF EDDY SHEDDING BY TOPOGRAPHY AND DEEP-WATER INFLOW THROUGH THE YUCATAN STRAITS

In this section the two-layer model is used to demonstrate a dramatic effect of topography on the eddy-shedding by the Loop Current when there is sufficient deep-water inflow through the Yucatan Straits. Fig. 11a shows the domain-averaged upper layer (upper curve) and lower layer kinetic energy vs. time for a two-layer experiment the same as shown in Fig. 4, except that during the first six years of model integration the lower layer inflow was zero. This includes the topography of Fig. 3. At the beginning of year 7 the lower layer inflow was increased to 10 Sv with a time constant of 30 days. While the lower layer inflow was zero, eddy shedding occurred in a manner similar to that shown in Fig. 4. The signature of the eddy shedding cycle is depicted in the upper layer energy curve of Fig. 11a. When the lower layer inflow was increased, the eddy shedding ceased and the solution evolved to a steady state as shown in Fig. 11a. This steady solution is shown in Fig. 11b, c in terms of the PA (Fig. 11b) and the lower layer pressure, p_2 (Fig. 11c). The PA depicts a source-sink flow like regime N, while the flow in the lower layer follows the f/h contours of the topography. HT uses a kinematic analysis to illuminate the dynamics of this phenomenon. From the continuity equation (2), the divergence term $h_1 \nabla \cdot w_1$ is balanced by the advective term $w_1 \cdot \nabla h_1$ in a steady state. Since the flow is nearly geostrophic, $w_1 \cdot \nabla h_1 \approx w_{1g} \cdot \nabla h_1 = w_{2g} \cdot \nabla h_1$, where w_{1g} is the geostrophic

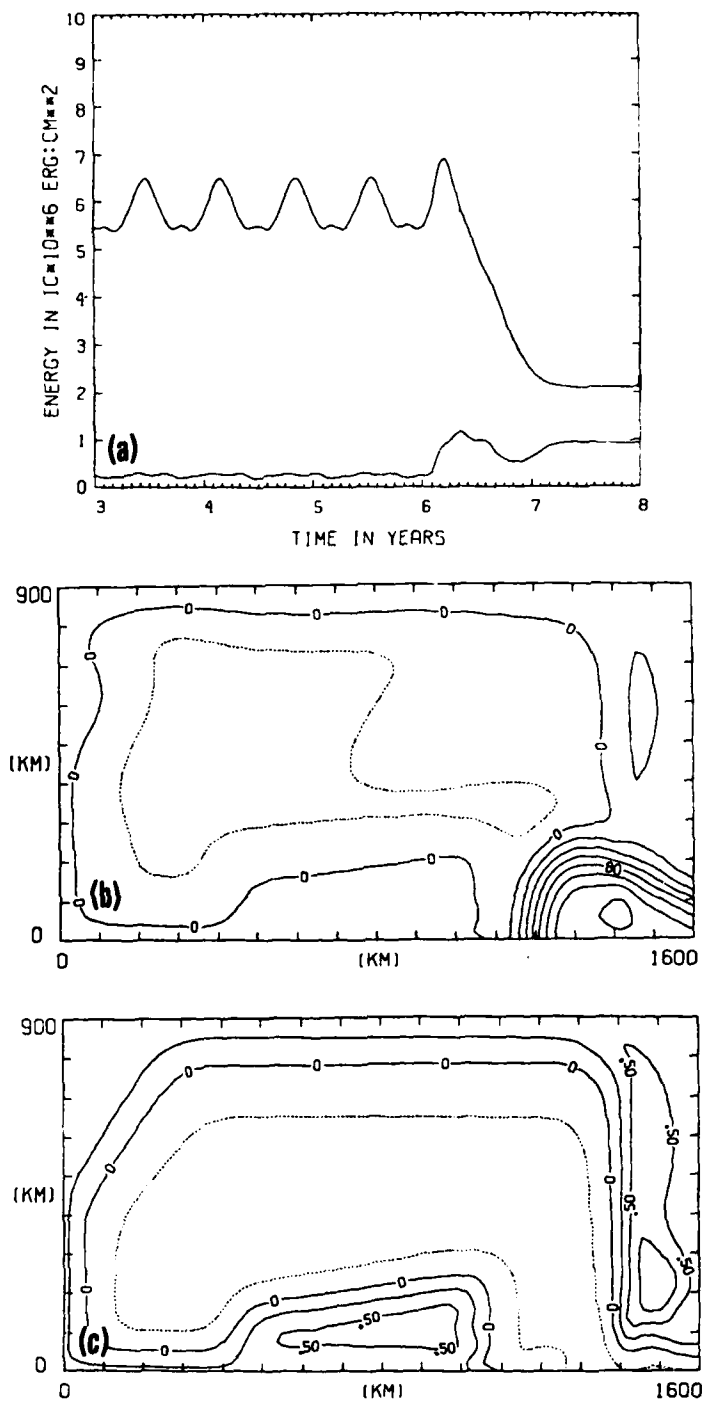


Fig. 11. Results for the bottom topography experiment shown in Fig. 4 except that $T_1 = 25 \text{ Sv}$ and $T_2 = 0$ until year 6 when T_2 increases to 10 Sv . (a) domain-averaged upper layer (top curve) and lower layer kinetic energy, ($IC = 1.5$). (b) Nearly steady PA at day 2880. The contour interval is 20 m . (c) Lower layer pressure normalized by density (p_2) at day 2880. The contour interval is $.25 \text{ m}^2/\text{s}^2$.

velocity component in layer i . The magnitude of $w_{2g} \cdot \nabla h_1$ is greatest when relatively strong lower layer currents flow at large angles to contours of h_1 . Comparison of Fig. 11b and 11c shows that this occurs where the Loop Current intersects a current following the f/h contours of the West Florida Shelf. If the lower layer current is strong enough for the advection to balance the divergence in (2) associated with the approaching Loop, then the interface deepening and Loop Current penetration in this region are halted.

Thus, the West Florida Shelf along the eastern boundary of the domain (see Fig. 3) and lower layer flow act in conjunction to effectively reduce the port separation by locally limiting the northward penetration of the Loop Current. If this results in $R_B \geq 2$, when we measure $2L_p$ as the distance between the center of the inflow port and the point where the upper and lower layer currents intersect, then the upper layer current exhibits the source-sink flow characteristic of the N regime described in Section 6. This is illustrated by comparing Fig. 11b with Fig. 9b, the reduced gravity experiment with a land mass in the location of the West Florida Shelf.

In the experiment shown in Fig. 11 the Loop Current had already penetrated far into the Gulf and shed eddies when the lower layer inflow was increased. When this increase occurred, a current following the f/h contours developed in the lower layer and the advection term ($w_1 \cdot \nabla h_1$) began to exceed the divergence term in the continuity equation where the Loop Current crossed the shelf slope, causing h_1 to decrease there. Thus, the Loop Current retreated southward until an equilibrium occurred near the southern end of the shelf.

In terms of vorticity dynamics, the northward penetration of the Loop Current is halted when the interaction between the topography of the West Florida Shelf and the pressure field results in a near balance between the pressure torques and the nonlinear terms in the mass transport vorticity equation. HT discuss and document this topic in more detail.

The results in this section suggest that certain time variations in the deep flow through the Yucatan Straits may have a greater effect on the Loop Current than fluctuations in the upper ocean current through the Strait. The effects of the latter are discussed by HT but not in this paper.

8. BAROTROPIC VS. BAROCLINIC INSTABILITY AND THE IMPORTANT ROLE OF TOPOGRAPHY

Section 6 examined stability regimes for the reduced gravity model. In Section 7 we studied a steady regime for the two-layer model which results from a particular combination of topography and deep flow following f/h contours. In this section we will investigate additional regimes of the two active layer model, confining ourselves to unsteady regimes with eddies. In particular we will search for cases of barotropic, baroclinic, and mixed instability.

The reduced gravity and barotropic models can exhibit barotropic, but not baroclinic instability. The reduced gravity model has demonstrated an eddy shedding regime with a horizontal shear instability of the first internal mode (a "barotropic" instability) which produces a remarkable simulation of observed features of the Loop Current - eddy shedding system. We know from Section 4 that in some cases the two active layer model exhibits similar results with similar parameters. In this section we will investigate the potential importance of baroclinic instability and the role of topography in determining its importance.

8.1 Eddy-mean energetics

We begin this investigation by surveying the eddy-mean energetics for the seven numerical experiments listed in Table 3. We then illustrate some characteristic features of the different regimes using synoptic maps of upper and lower layer pressure (p_1 and p_2) and curves of domain-averaged energy vs. time. Fig. 12 shows the eddy-mean energetics in terms of energy box diagrams. Fig. 12a labels the energy transfers. See Appendix A for symbol definitions and Appendix C for the energy transfer integrals. All of the model domain was used in calculating the energetics except the parts within 100 km of the eastern boundary and 37.5 km of the southern boundary. Thus, the eastern and southern boundaries of the energetics calculations are open. Kinetic energy and pressure work fluxes through these open boundaries are represented by arrows at the top (bottom) of the K_1 (K_2) boxes. In all cases most of the energy flows into \bar{K}_1 . In some cases there is significant efflux from K_1' , but always must less than the $\bar{K}_1 \rightarrow K_1'$ transfer. The arrows pointing outward from the sides represent dissipation of a particular type of energy due to Laplacian horizontal friction. Arrows between the boxes represent conversions of energy from one type to another as indicated by the direction of the arrow.

Fig. 12b shows the eddy-mean energetics for Experiment 1 on Table 3, a two-layer flat-bottom experiment using the standard parameters given in Table 1. The $\bar{K}_1 \rightarrow K_1'$ energy conversion is characteristic of a barotropic instability. The potential energy transfer is actually reversed with eddy potential energy (P') feeding the mean.

Angling the inflow 27° west of normal in the standard two-layer flat-bottom model (Experiment 2) produced a dramatic change in the eddy-mean energetics which

TABLE 3
Model experiments discussed in Section 8

Exp #	Differences from standard two-layer flat-bottom experiment in Table 1	Figures in HT from these experiments (HT Fig. #)
1	None	Figs. 5b, 11b, 14a
2	$\theta_I = 27^0$, $Sv_2 = 0$	Figs. 12, 13a, 14d
3	Reduced gravity, Yucatan and Florida Straits added to model domain	Figs. 20a, 21a, HT Table 2 case RG32
4	$A = 3 \times 10^6 \text{ cm}^2/\text{s}$, $Sv_2 = 0$	Experiment in HT Figs. 10, 11a, 14c exhibits similar behavior
5	$A = 3 \times 10^5 \text{ cm}^2/\text{s}$, $Sv_2 = 0$ Fig. 3 topography	
6	$Sv_1 = 25$, $Sv_2 = 0$	Figs. 24b, 25b
7	$Sv_1 = 25$, $Sv_2 = 0$, Fig. 3 topography	Figs. 24c, 25c

Sv_i is the inflow in layer i in $10^6 \text{ m}^3/\text{s}$ or Sv .

is shown in Fig. 12c. (The lower layer inflow was also reduced to zero, but other experiments show this has a relatively minor role in altering the energetics in this case). Fig. 12c illustrates a classic signature of baroclinic instability in the eddy-mean energetics with $\bar{P} \rightarrow P'$ dominating the mean to eddy energy transfer and feeding the upper and lower layers almost equally. There is even a reverse cascade in the kinetic energy ($K_1 \rightarrow \bar{K}_1$) with eddies feeding the mean flow.

The eddy-mean energetics for the reduced gravity model (Experiment 3 and Fig. 12d) illustrates a pure barotropic instability, since this model excludes baroclinic instability. In this case the dominant mean to eddy energy transfer is $\bar{K} \rightarrow K'$. Even though this is a pure barotropic instability, there is a net transfer from $\bar{P} \rightarrow P'$. Thus, the existence of such a transfer does not necessarily imply any contribution from baroclinic instability.

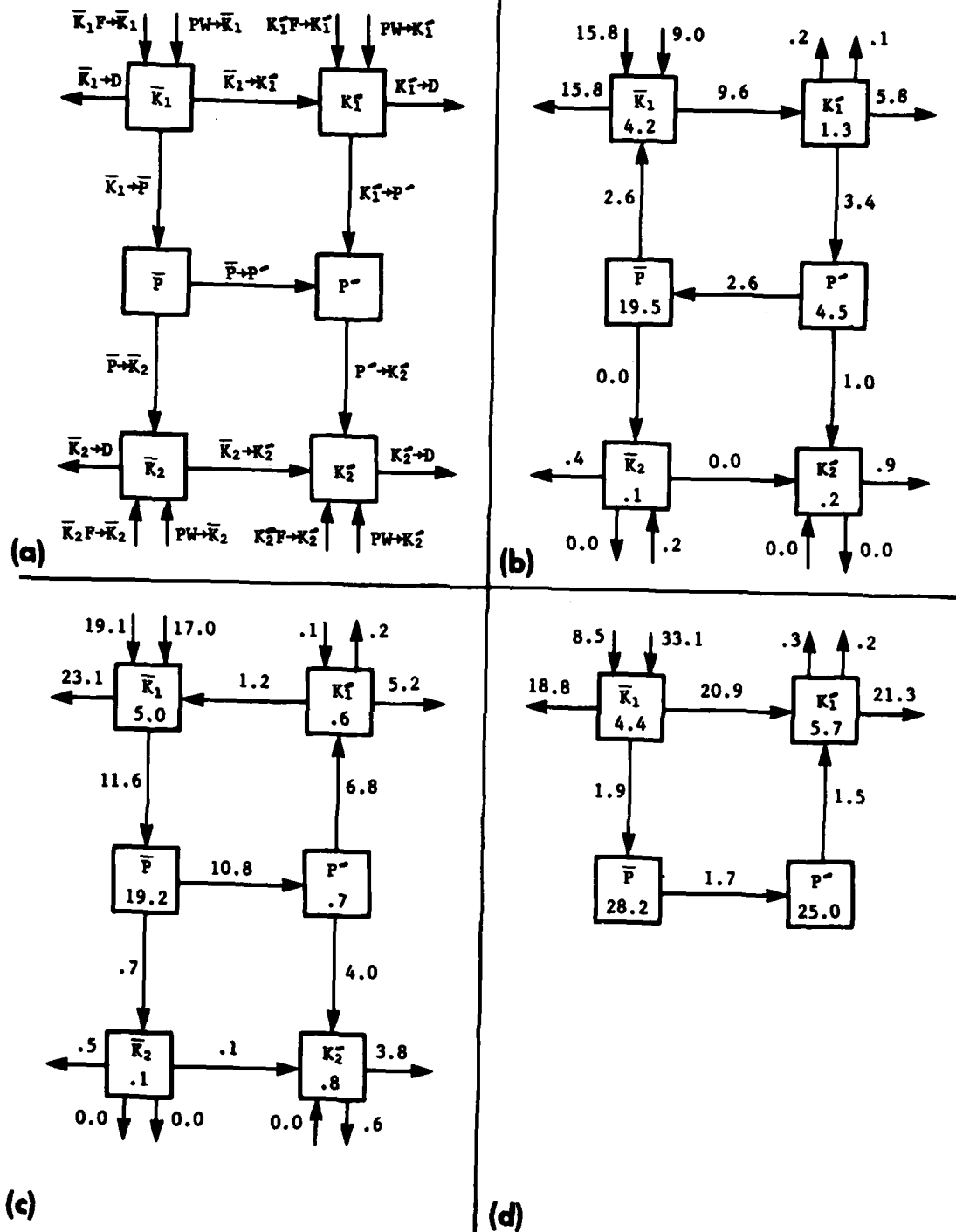
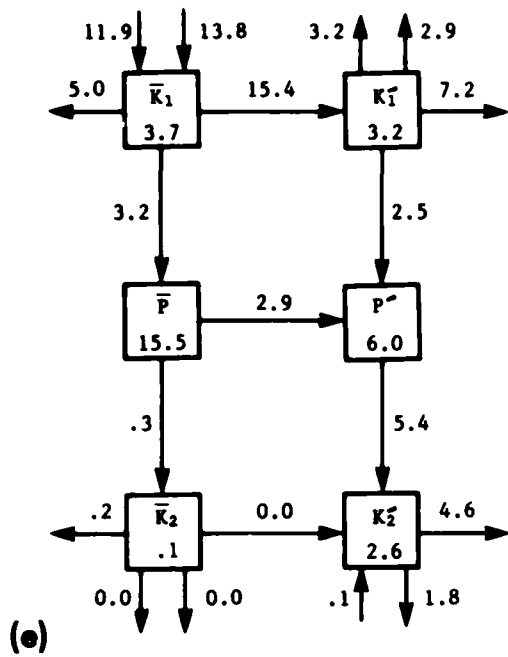
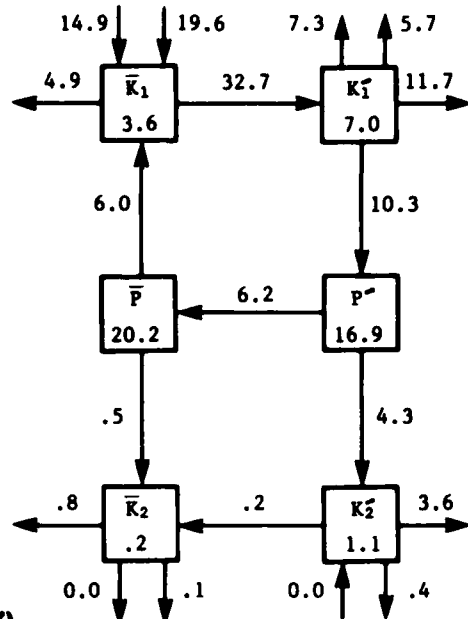


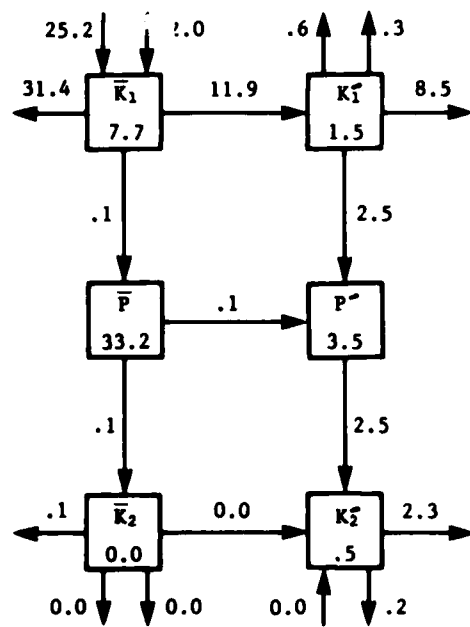
Fig. 12. Eddy-mean energetics for the experiments listed in Table 3: (a) labels for the energy pathways and energy reservoirs, (b) energetics for Experiment 1, standard flat-bottom case, (c) Experiment 2, flat bottom with non-normal inflow, (d) Experiment 3, reduced gravity, (e) Experiment 4, flat bottom with low



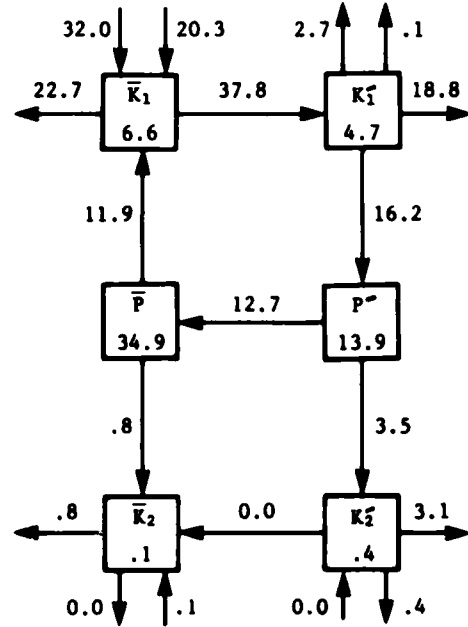
(e)



(f)



(g)



(h)

viscosity, (f) Experiment 5, same as the preceding but with topography, (g) Experiment 6, flat bottom, (h) Experiment 7, same as preceding but with topography. The energy reservoirs are in units of 10^{15} joules and the energy transfers are in units of 10^8 joules/s.

Fig. 12e is particularly interesting because it illustrates a mixed instability and because it demonstrates the value of separating the kinetic energy into upper and lower layer components. These results were obtained primarily by reducing the eddy viscosity in the two-layer flat-bottom model by a factor of three (Experiment 4). If K_1 and K_2 were combined to produce a 4-box diagram, the results would look much like those for the reduced gravity model and we might conclude that this is a case of barotropic instability. In contrast, the 6-box diagram (Fig. 12e) illustrates a striking result. Although a barotropic energy conversion ($\bar{K}_1 \rightarrow K_1'$) is dominant in the upper layer, the lower layer eddies are fed almost equally by transfers from $\bar{P} \rightarrow P'$ and $K_1' \rightarrow P'$. In view of the reduced gravity results, this is insufficient evidence for an important contribution from baroclinic instability to the lower layer eddies. Additional evidence for this will be provided shortly.

Figs. 12e and 12f compare the results for Experiments 4 and 5. The experiments are identical except that Experiment 4 (Fig. 12e) has a flat bottom and Experiment 5 (Fig. 12f) includes the idealized Gulf of Mexico topography shown in Fig. 3. The topography strongly suppresses any baroclinic instability. With the topography added, the energy box diagram (Fig. 12f) indicates a strong barotropic instability ($\bar{K}_1 \rightarrow K_1'$) and a strong reverse potential energy flux ($P' \rightarrow \bar{P}$).

Figs. 12g and 12h again compare experiments with and without the topography of Fig. 3 (Experiments 6 and 7). They differ from the preceding by a three-fold increase in the eddy viscosity and a 25% increase in the upper layer inflow. The experiment with the topography (Fig. 12h) exhibits essentially the same energy pathways as the previous frame with the same topography (Fig. 12f). The reverse potential energy transfer ($P' \rightarrow \bar{P}$) is even stronger. Almost 1/3 of the eddy energy makes a complete circuit. Although this reverse transfer is clearly augmented by the topography, it is not restricted to experiments with topography (see Fig. 12b). Without the benefit of the energetics analysis, HT correctly identified the baroclinically unstable case (Fig. 12c) and a mixed instability case similar to Fig. 12e. However, they also conjectured that Experiment 6 (Fig. 12g) is a case of mixed instability. This is not corroborated by the domain integrated eddy-mean energetics. Eddies in both layers are fed by energy

conversions appropriate for a barotropic instability, the lower layer fed indirectly via energy transfer from the upper layer. In this case, increasing the eddy viscosity has suppressed the contribution from baroclinic instability. Experiment 6 (Fig. 12g) differs from Experiment 1 (Fig. 12b) by having 25% greater inflow in the upper layer and none in the lower layer. The energy pathways in the two experiments are similar, but Fig. 12g shows more energy transfer to the lower layer and lacks the reverse ($P' \rightarrow \bar{P}$) transfer of the standard flat-bottom experiment (Fig. 12b).

The energy transfers in all these experiments are strongly inhomogeneous in space. Thus, as stressed by Harrison and Robinson (1978), energy transfers averaged over the model domain may not be characteristic of any important subregion.

8.2 Kinetic energy vs. time

In the following discussion, we will illustrate features of the flow which are characteristic of the three regimes identified in the eddy-mean energetics with barotropic, baroclinic, and mixed instabilities. We will utilize the four experiments which do this most simply and clearly, (a) Experiment 1 for barotropic instability with a flat bottom, (b) Experiment 7 for barotropic instability with topography, (c) Experiment 2 for baroclinic instability, and (d) Experiment 4 for mixed instability. Fig. 13 shows the curves of K_1 and K_2 vs. time for these four experiments.

Fig. 13a, b represents the barotropically unstable experiments and clearly shows a relatively long period for the eddy shedding cycle, 273 days for Experiment 1 (Fig. 13a) and 250 days for Experiment 7 (Fig. 13b). Fig. 13c shows a much faster 57 day oscillation for the baroclinically unstable experiment, Experiment 2. The corresponding reduced gravity experiment (not shown), in which baroclinic instability is not permitted, has a 284 day period. The period in Fig. 13c is very similar to that found by Holland and Lin (1975) for mid-latitude mesoscale eddies in a two-layer model with baroclinic instability. They also noted a similar maximum in K_1 near the onset of baroclinic instability which is followed by a rise in K_2 . We have not found this type of signature in any of our barotropically unstable experiments. Fig. 13d shows K_1 and K_2 vs. time for Experiment 4, the experiment for which the eddy-mean energetics (Fig. 12e) suggest a mixed instability. Two periods which are not harmonically related are clearly indicated, a long period of 300 days, which is typical of barotropically unstable experiments, and a much shorter 56 day period similar to that for the baroclinically unstable experiment. Also notable are the dramatic spikes in K_2 lagging the maximum in K_1 . This resembles the behavior of K_2 at the onset of baroclinic instability shown in Fig. 13c.

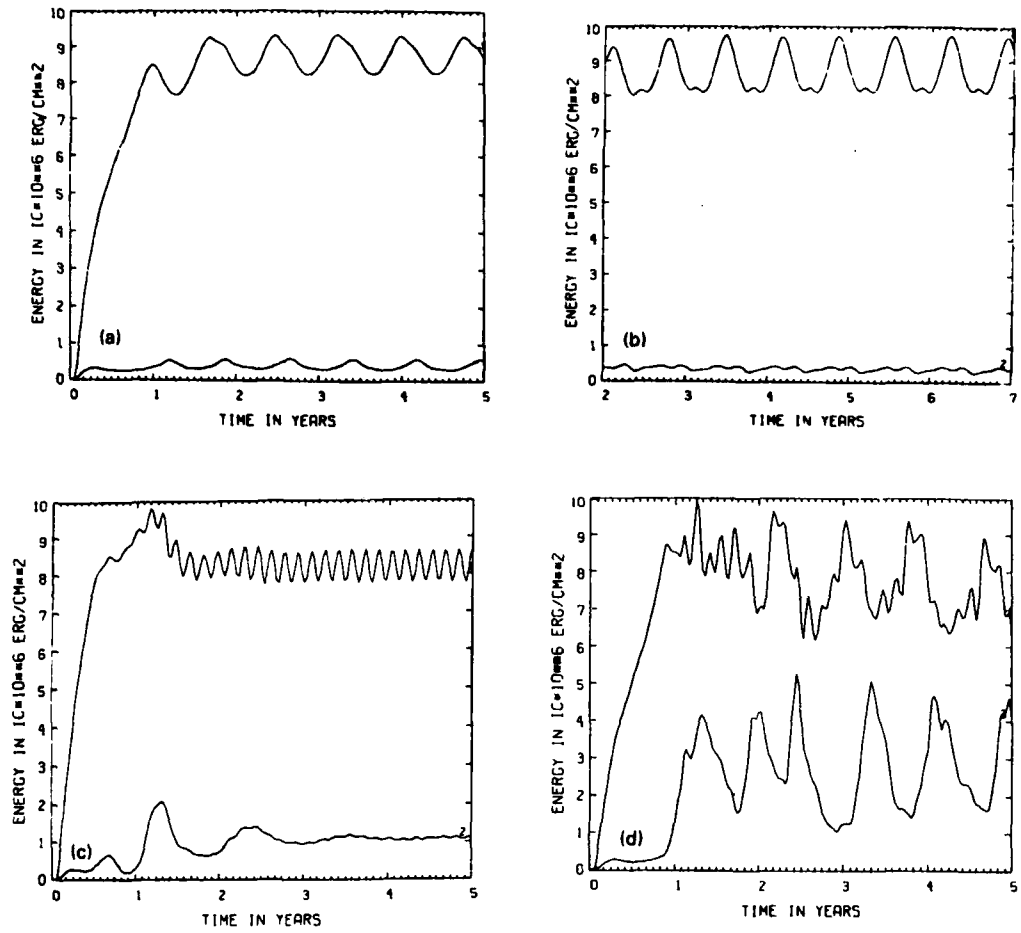


Fig. 13. Average kinetic energy over the rectangular domain (upper curve for upper layer) for (a) Experiment 1, the standard two-layer flat-bottom case, (b) Experiment 7, with the topography of Fig. 3, (c) Experiment 2, with non-normal inflow, and (d) Experiment 4, identical to Experiment 1 but with $A = 3 \times 10^6 \text{ cm}^2/\text{s}$ and $Sv_2 = 0$. The value of IC is (a) .5, (b) 1.0, (c) .55, (d) .7.

8.3 Modon generation in the barotropically unstable experiments

We begin examining the characteristic features of the flow in different regimes by studying two experiments where the eddy-mean energetics indicate barotropic instability. One experiment has a flat bottom, and the other includes the idealized Gulf of Mexico topography shown in Fig. 3. The two experiments which illustrate the basic features of this flow in the simplest and clearest fashion are Experiment 1 with Fig. 12b energetics (the standard flat-bottom experiment) and Experiment 7 with topography and Fig. 12h energetics.

Fig. 14 shows synoptic views of p_1 and p_2 for Experiment 1. At day 1710, p_1 (Fig. 14a) shows the Loop Current penetrating into the basin and beginning to bend westward. An eddy shed earlier lies in the western Gulf. A characteristic feature of the barotropically unstable experiments is the generation of a modon in the lower layer as the Loop Current begins to form an eddy (Fig. 14b). The relationship between p_1 and p_2 can be seen clearly by superimposing the fields. The modon intensity tends to follow that of the generating eddy in the upper layer. The axis of the modon is oriented close to the direction of propagation by the upper layer vortex with the anticyclonic member leading and the cyclonic member trailing. The orientation of the modon generated here is quite different from that found by McWilliams and Flierl (1979) for isolated, nearly circular vortices, but the tendency of the eddy in the upper layer to propagate toward the member of the modon with like rotation is similar. However, in this case the westward propagation speed of the modon slightly exceeds that of the upper layer vortex. Thus the flow actually becomes more baroclinic and in Fig. 14a, b we see the anticyclonic eddy in the upper layer situated over the cyclonic member of the modon. This behavior is common but not universal in our numerical experiments. It is quite unlike the coupled behavior of the isolated baroclinic vortex and barotropic modon studied by McWilliams and Flierl (1979). In their results the modon member with rotation unlike the baroclinic vortex eventually broke away and the barotropic and baroclinic vortices tended to become superimposed and to approach a state of deep compensation (no signature of the vortex in the lower layer). When the upper layer vortex reaches the western boundary and propagates northward (Fig. 14c), it is again associated with a modon in the lower layer (Fig. 14d) and again the modon is oriented in the direction of propagation with the like (anticyclonic) member leading and the opposite member trailing.

Fig. 14b, d shows an additional interesting phenomenon which occurs in the lower layer. If the lower layer were integrated separately as a barotropic model, the solution would evolve to a steady, westward-bending Loop Current as in regime W. The solution would be similar to Fig. 8a but the loop would bend westward at a lower latitude because $(v_c/\beta)^{1/2}$ is much less (see Section 5.5).

- The lower layer inflow velocity at the core of the current is only 3.35 cm/sec.

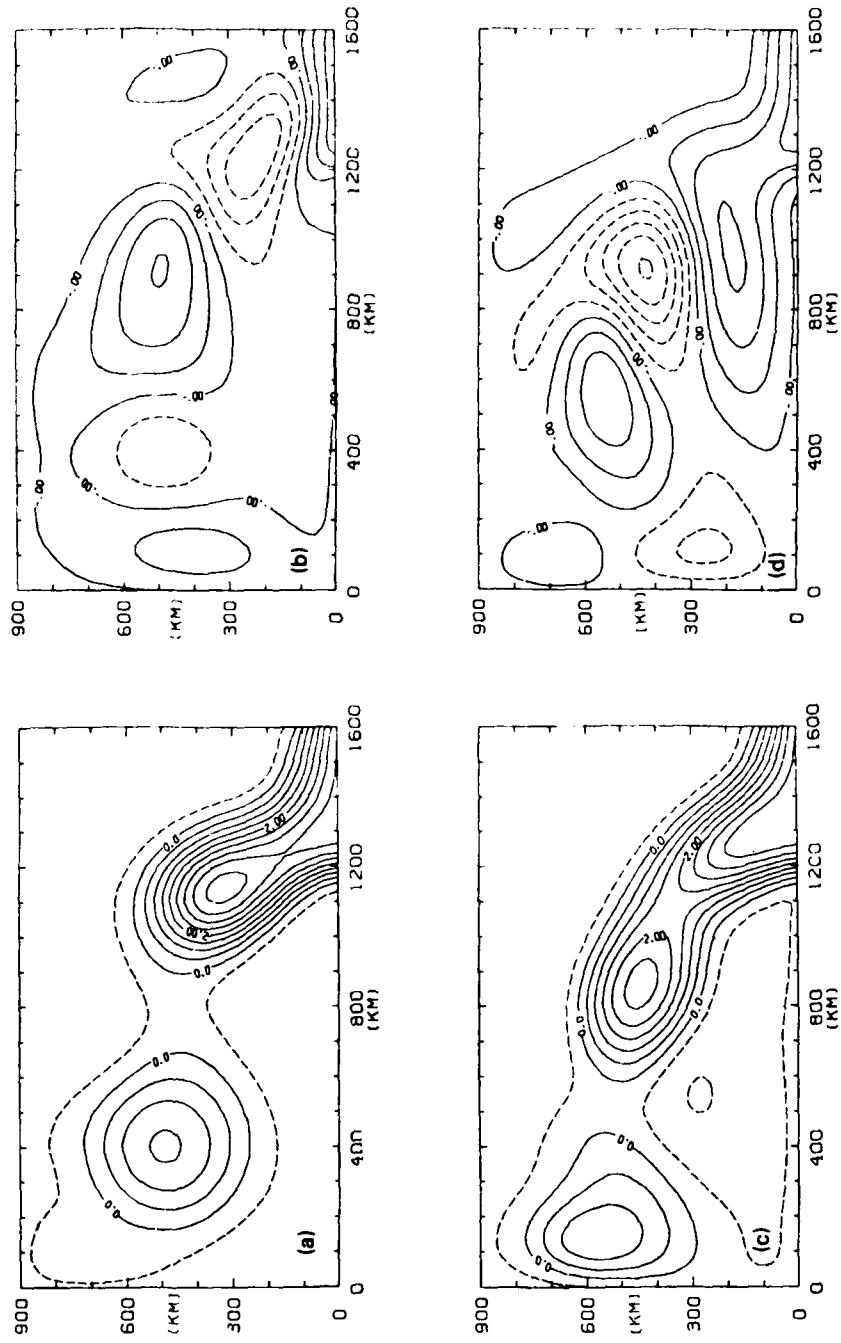


Fig. 14. (a) p_1 and (b) p_2 at day 1710 and (c) p_1 and (d) p_2 at day 1800 for Experiment 1. The contour interval is $.5 \text{ m}^2/\text{s}^2$ for p_1 and $.05 \text{ m}^2/\text{s}^2$ for p_2 .

In this experiment with two active layers, the lower layer flow is quite different from the barotropic prediction. During the formation of the modon, the Loop Current in the lower layer exhibits a source-sink flow (Fig. 14b). The modon is the dominant flow and prevents the natural westward bending of the Loop. When the modon moves away (Fig. 14d), the lower layer Loop bends far to the west and sheds a weak eddy almost in phase with the upper layer (Fig. 14c). In the mean (Fig. 15) both the upper and lower layers exhibit a westward-bending loop like the W regime. As predicted by $(v_C/\beta)^{1/2}$ and the higher inflow velocity in the upper layer, the mean loop in the upper layer bends westward at a higher latitude. The lower layer also exhibits counter-rotating and zonally elongated mean gyres north of the loop. These are driven by downward flux of eddy energy from the upper layer and may also influence the latitude of the mean Loop Current in the lower layer.

Fig. 16 shows a synoptic view of p_1 and p_2 at day 1760 for a barotropically unstable experiment with Fig. 3 topography (Experiment 7 with Fig. 12h energetics). This experiment exhibits coupled upper layer vortex, lower layer modon behavior similar to the flat bottom experiment, except that the modon is mostly confined to the abyssal plain. Another difference is that the upper layer vortex remains between the modon pair. The modon is partially steered by the topography. Apparently, the back interaction from the modon to the upper layer is sufficient that the trajectory of the upper layer vortex is also modified by the topography. Fig. 17 compares upper layer eddy trajectories for Experiments 6 and 7, two experiments with no flow through the ports in the lower layer. The experiments are identical except that Experiment 6 has a flat bottom and Experiment 7 includes Fig. 3 topography. Because Experiment 7 includes no flow through the ports in the lower layer, there is no current following the f/h contours, unlike Fig. 11c. The addition of such a current had no major effect on the modon, provided the current was weak enough to permit the normal eddy shedding to occur.

Although eddy activity in the lower layer modified the propagation of the upper layer vortex, the propagation of both the upper layer vortex and the associated modon was dominated by internal Rossby wave propagation in both the reduced gravity and two active layer experiments which exhibited discrete eddy shedding and a horizontal shear (barotropic) instability of the internal mode. As we will see shortly, this is not the case in the experiment with a baroclinic instability.

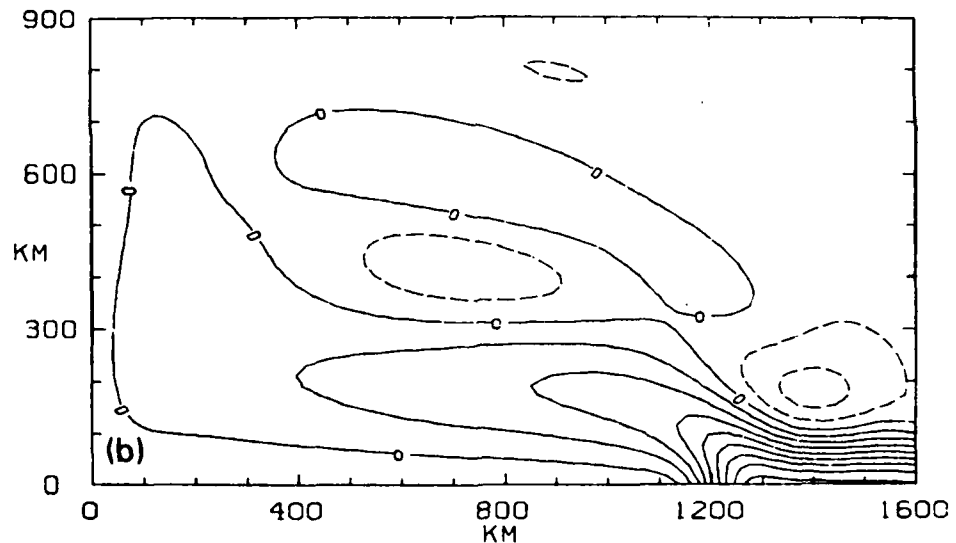
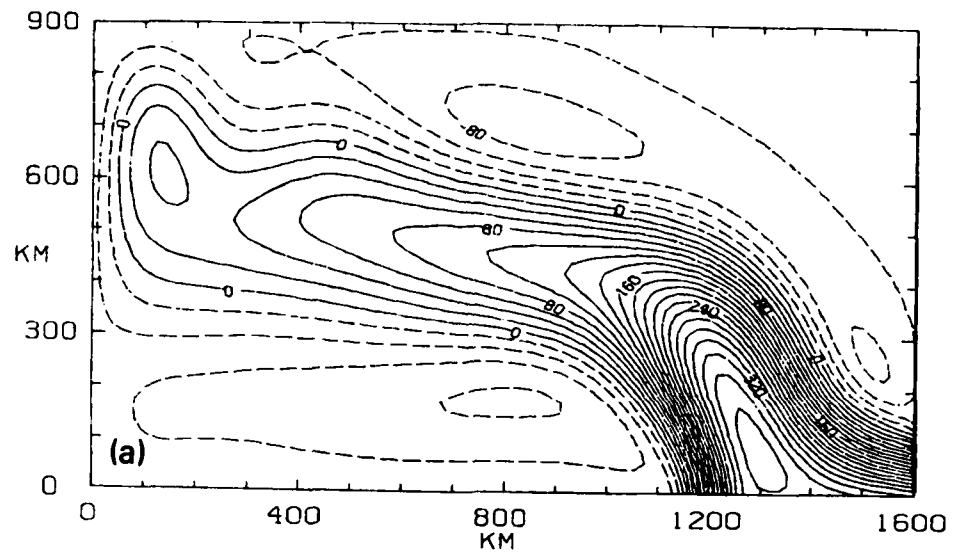


Fig. 15. Time mean of (a) p_1 and (b) p_2 for Experiment 1. The contour interval is $.2 \text{ m}^2/\text{s}^2$ for p_1 and $.02 \text{ m}^2/\text{s}^2$ for p_2 .

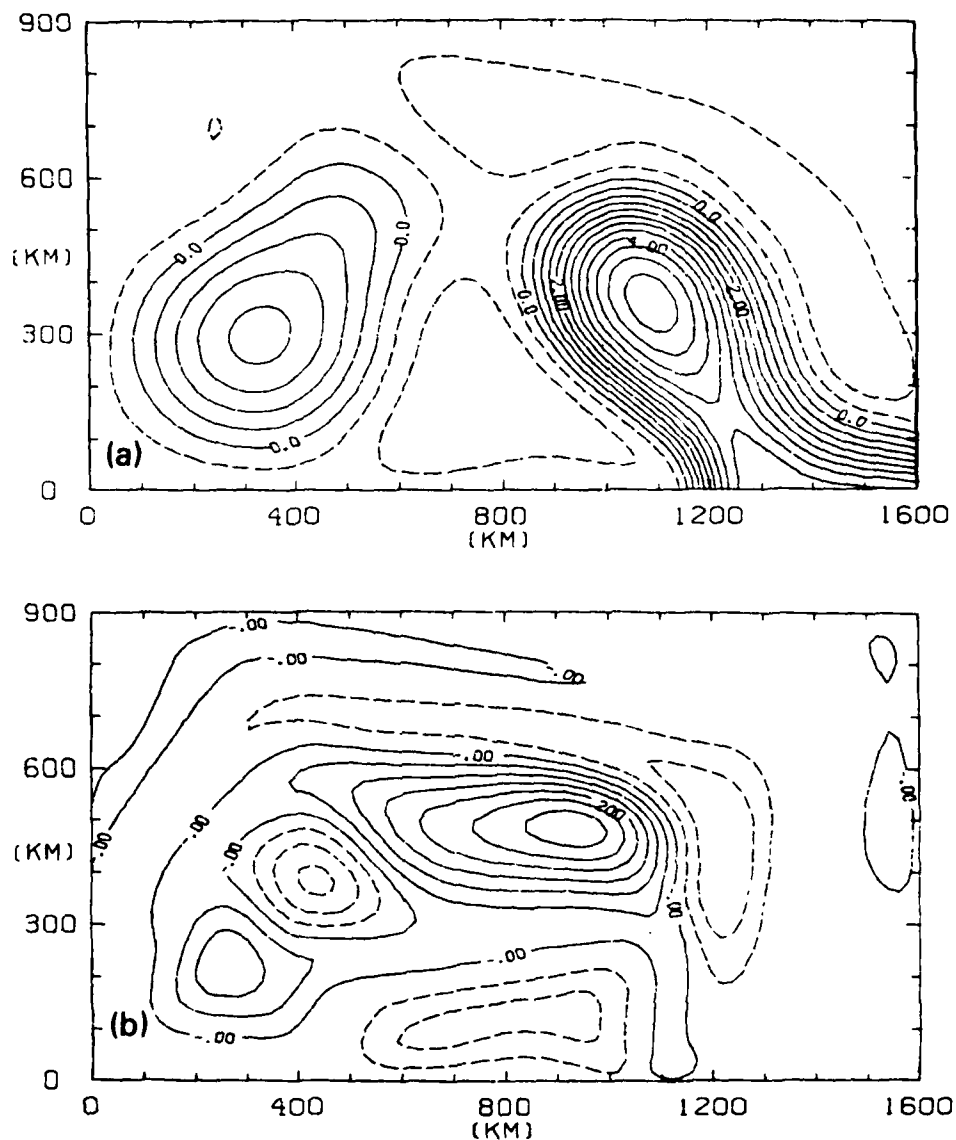


Fig. 16. (a) p_1 and (b) p_2 at day 1760 for Experiment 7. The contour interval is $.5 \text{ m}^2/\text{s}^2$ for p_1 and $.05 \text{ m}^2/\text{s}^2$ for p_2 .

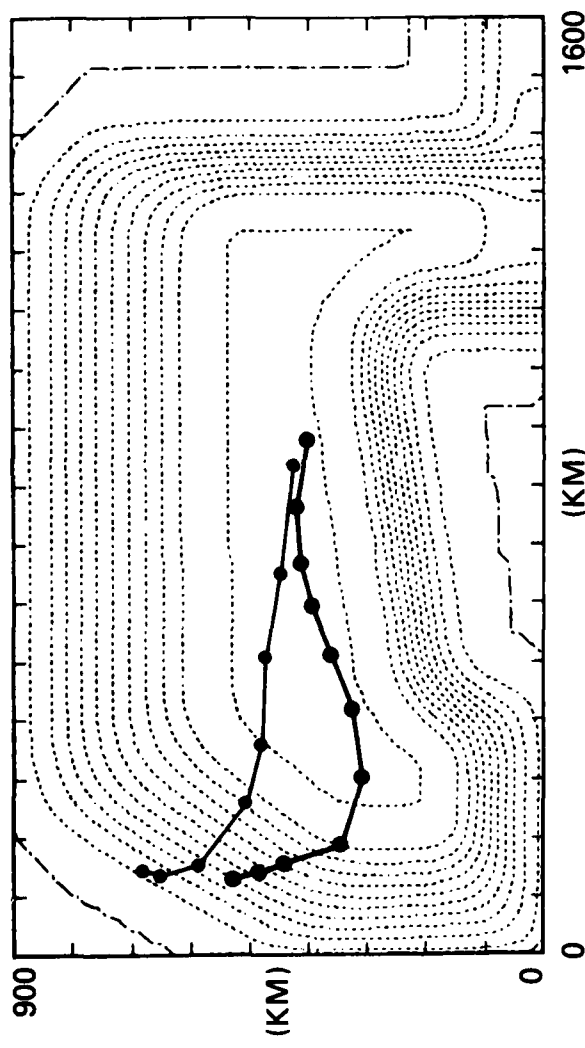


Fig. 17. Shows the effect of bottom topography on eddy trajectories for identical experiments except that Experiment 6 (upper trajectory) had a flat bottom and Experiment 7 (lower trajectory) included the topography of Fig. 3 which is used as background in this figure. The trajectories are dotted at 30 day intervals.

8.4 Flow characteristics associated with baroclinic instability

Fig. 18 shows a synoptic view of p_1 and p_2 for Experiment 2 where the upper layer inflow is angled 27° west of normal and there is no flow through the ports in the lower layer. The eddy-mean energetics (Fig. 12c) indicate the occurrence of baroclinic instability. This experiment exhibits modon-like generation similar to that earlier associated with a barotropic instability. However, the eddies tend to be smaller and the greater population of eddies tends to mask the modon character of the eddy generation. The upper and lower layer eddies near the eastern part of the Loop bear a phase relationship which is similar to the barotropically unstable experiments. The modon axis is oriented close to the direction of propagation of the anticyclonic eddy in the upper layer, with the anticyclonic modon member leading and the cyclonic one trailing. One difference is that the modon axis is south of the upper layer vortex. Thus, the lower layer eddies tend to be strongest under the westward-flowing arm of the Loop Current as expected for a baroclinic instability (Gill, et al, 1974; Philander, 1976). Later, in the central basin the leading modon member shifts northward, away from the westward propagating vortex in the upper layer. The trailing vortex remains under the westward branch of the Loop. Thus the modon axis is no longer aligned with the direction of propagation. In general, the lower layer eddies tend to be elongated meridionally in the eastern part of the basin where they originate and zonally in the western part of the basin where they decay. In the western part of the basin the eddies also show some tendency toward barotropy. Except for the initial meridional elongation, these tendencies are consistent with results presented by Rhines (1977).

The most dramatic difference between the experiments with barotropic and baroclinic instability lies in the propagation speed of the eddies. In the barotropically unstable experiments with discrete eddies the internal Rossby wave speed associated with the upper layer vortex exerts primary control on the propagation in both layers. Even though the eddies in the baroclinically unstable case are smaller, they propagate westward at ~ 10 cm/sec, typically 2 to 3 times faster than in the barotropically unstable experiments. Although it is difficult to estimate an appropriate shear velocity, the propagation speeds in our numerical model are quite consistent with those for baroclinic instability in a linearized two-layer model with a horizontally uniform basic flow (Pedlosky, 1979).

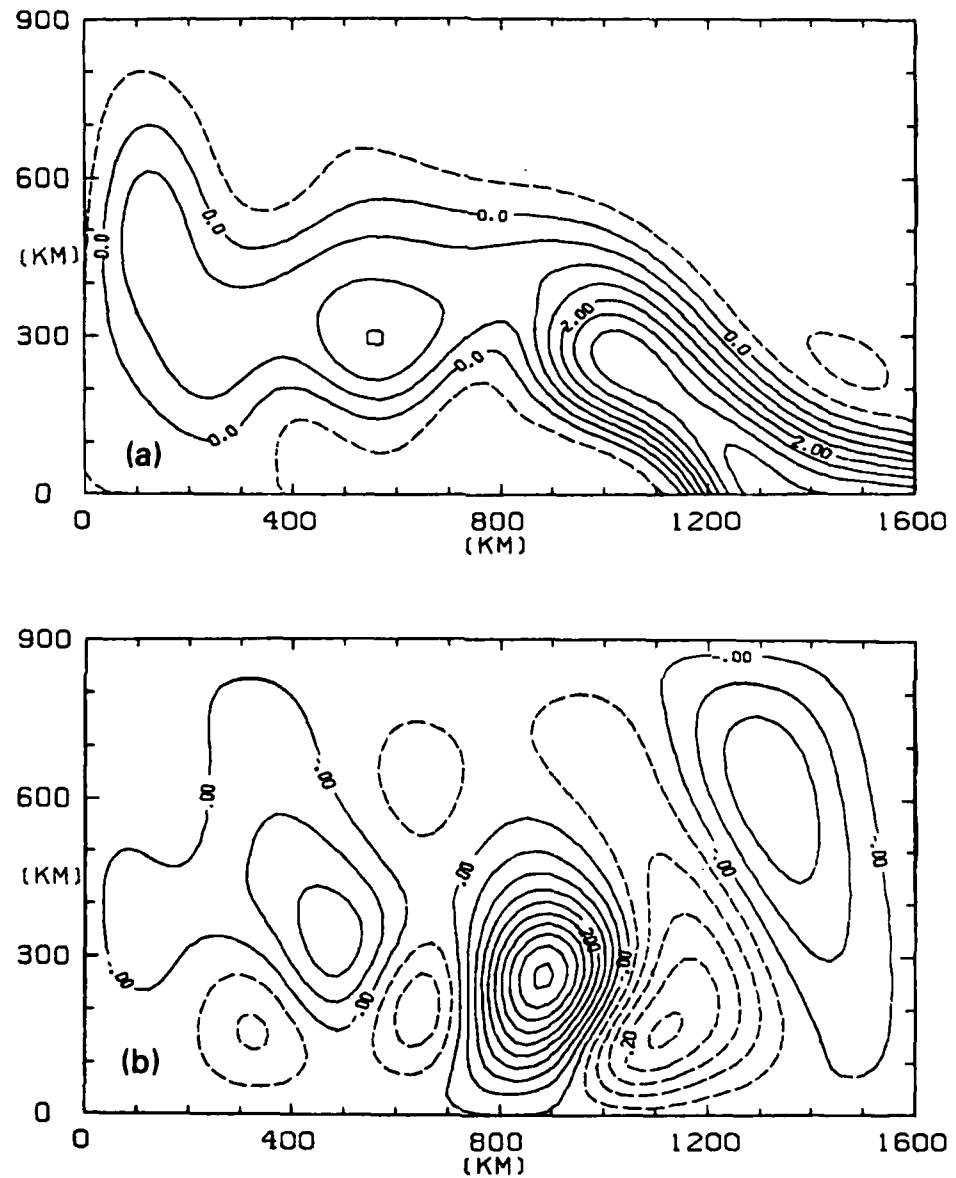


Fig. 18. (a) p_1 and (b) p_2 at day 2450 for Experiment 2. The contour interval is $.5 \text{ m}^2/\text{s}^2$ for p_1 and $.05 \text{ m}^2/\text{s}^2$ for p_2 .

Gill, et al (1974) have suggested the upper to lower layer phase shift as a means of detecting baroclinic instability. In our results we find this is not very useful because the barotropic instability which occurs in the upper layer generates a modon in the lower layer with upper-lower layer phase relationships which are much like those of the baroclinic instability. In our results the westward propagation speed of the eddies is a much clearer distinguishing characteristic.

8.5 Flow characteristics of a mixed instability

Fig. 19 shows two synoptic views of p_1 and p_2 for Experiment 4 which has a flat bottom, no inflow in the lower layer, and one-third the eddy viscosity of the experiments discussed in Sections 8.3 and 8.4. The eddy-mean energetics (Fig. 12e) suggest that a mixed instability occurs in this experiment. Since there is no flow through the ports in the lower layer, all the energy in the lower layer is received from the upper layer. Apart from this the flows in the two layers are much more independent than those discussed in the two preceding subsections.

Eddies in the lower layer propagate westward at approximately the external Rossby wave speed (~ 10 cm/sec), and those with like rotation pass a given point with a periodicity of about 60 days. Unlike the experiments discussed in Sections 8.3 and 8.4 there is no clear phase relationship between the eddies in the lower layer and the eddy which forms on the Loop Current in the upper layer. This is true during most, but not all, of the eddy-shedding cycle of the Loop Current. In this experiment the eddy-shedding period is about 300 days and is depicted as a slow oscillation in K_1 (Fig. 13d). There is a back interaction from the lower layer eddies to the Loop Current in the upper layer which causes a strong undulation of the Loop with approximately a 60 day period. This is depicted in Fig. 13d as the high frequency oscillation in K_1 . Except for this undulation, the Loop Current penetrates into the Gulf, bends westward and begins to form an eddy structure just as in the barotropically unstable experiments, but near the time an eddy would break off (Fig. 19a) in a barotropically unstable experiment, something quite different occurs. The Loop Current suddenly shoots far to the west at a speed appropriate for baroclinic instability and breaks into a series of smaller eddies. During this process lower layer eddies under the south side of the Loop strengthen dramatically and the upper and lower layer eddies develop distinct phase relationships. An anticyclonic eddy in the lower layer leads the westward advance on the Loop Current. At this stage phase relationships in the upper and lower layers are very similar to those for the baroclinically unstable case, and they exhibit the same differences from the barotropically unstable experiments. These phase relations disintegrate as soon as the rapid westward advance of the Loop Current is halted. Thus we have a

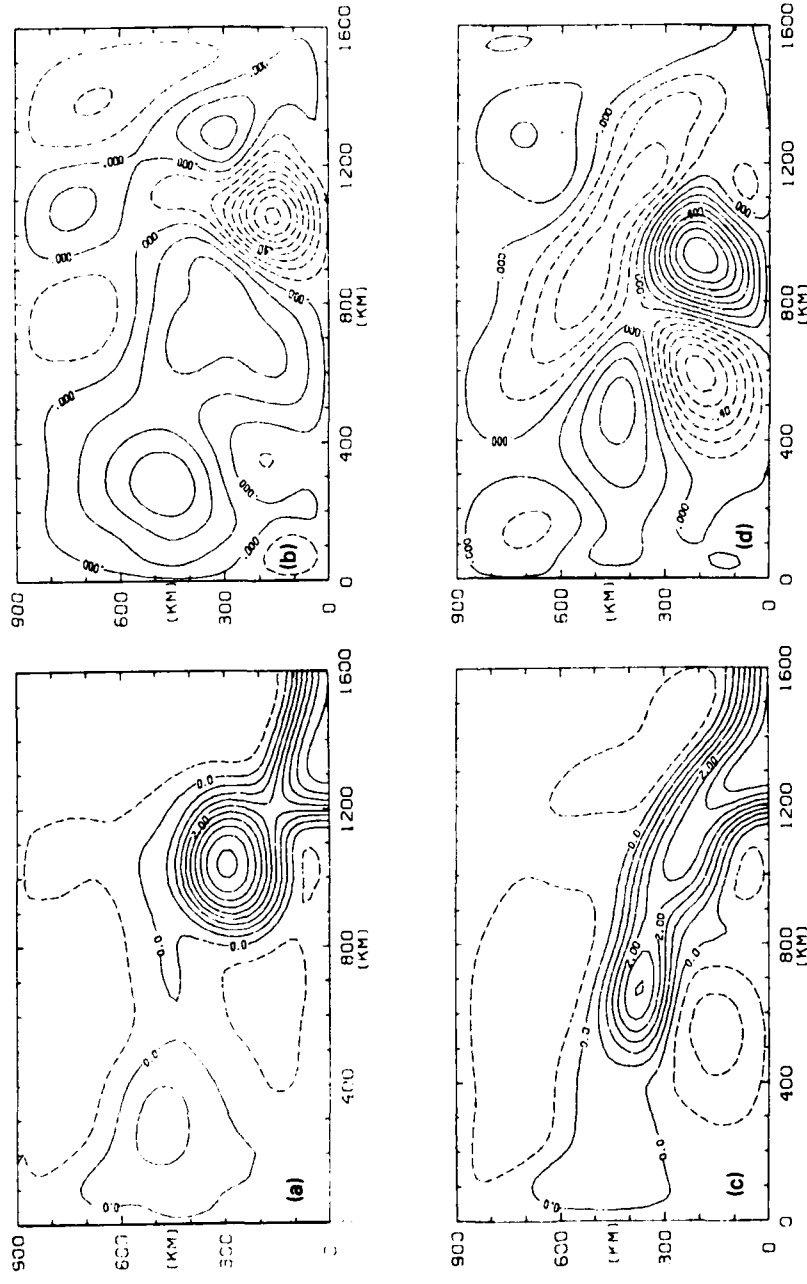


Fig. 19. (a) p_1 and (b) v_2 at day 1720 and (c) p_1 and (d) p_2 at day 1750 for Experiment 4. The contour interval is $.5 \text{ m}^2/\text{s}^2$ for p_1 and $.1 \text{ m}^2/\text{s}^2$ for p_2 .

picture of episodic baroclinic instability associated with a small part of each 300 day eddy-shedding cycle of the Loop Current. This instability is strong enough to show up in the domain-averaged eddy-mean energetics (Fig. 12e) and to provide a sharp spike in the curve of K_2 vs. time (Fig. 13d). Day 1720 (Fig. 19b) is near the foot of the last spike and day 1760 (Fig. 19d) is near the top of it.

The much weaker coupling for the two layers than found in either the barotropically or baroclinically unstable experiments is explained in part by the peculiar episodic nature of the baroclinic instability in Experiment 4 and in part by the 3 times lower eddy viscosity. Because the eddies in the lower layer are governed by external Rossby wave propagation, they are dispersive in nature. With the lower eddy viscosity they are not dissipated as soon after generation and have greater opportunity to disperse and fill the basin. The importance of dispersion in spreading the eddy population in the lower layer has been noted by Rhines (1977) and in the study of isolated vortices by McWilliams and Flierl (1979).

A comparison of Fig. 16 (for the experiment with idealized Gulf of Mexico topography) and Fig. 19 (for the flat-bottom experiment with a mixed instability) indicates how the topography can suppress the episodes of baroclinic instability found in the latter case. When the topography of Fig. 3 is present, the eddies in the lower layer are mostly confined to the abyssal plain. Lower layer eddy generation over the strongly sloping topography is prevented because the eddy flow would have to cross the closely packed f/h contours at large angles, behavior not anticipated in geostrophically balanced flow which conserves potential vorticity. The strong eddies in Fig. 19d which form under the westward-flowing branch of the Loop Current lie over the region of the Campeche Bank and the slope of the bank. Thus, they are prevented from forming when the topography of Fig. 3 is included. We can now appreciate why the two-layer model with topography produces results more like the reduced gravity model than does the two-layer flat-bottom model. If the westward branch of the Loop Current were to flow over the abyssal plain, we might expect the model to exhibit episodes of baroclinic instability even when the topography is included.

9. SUMMARY AND CONCLUSIONS

In this paper we have demonstrated the ability of simple numerical models to perform remarkable simulations of the Loop Current - eddy system in the Gulf of Mexico. The models were designed for computational efficiency and simplicity, retaining only the essential physics and characteristics of the Gulf required to simulate the basic dynamical behavior of the system. The simplicity of the models facilitated the analysis of the system dynamics and the computational efficiency allowed us to perform over 150 multi-year integrations. The efficiency also allowed us to use horizontal resolution adequate to investigate interesting regions of the parameter space, regions where time dependent eddies dominated the circulation.

The numerous numerical experiments explored the model parameter space and aided in the formulation and testing of dynamical hypotheses. The most salient results from the model are summarized in the seven points which follow.

1) The simple models were able to simulate the anticyclonic eddy shedding by the Loop Current and to simulate eddies with realistic diameters, amplitudes, and westward propagation (Figs. 1,4). Most striking was the ability of the models to simulate the observed quasi-annual period of the eddy shedding with no time variations in the inflow through the Yucatan Straits (southern port). This is contrary to the popular hypothesis that the Loop Current sheds eddies in response to annual variations of the inflow.

2) The reduced gravity model proved to be the simplest model able to simulate the basic dynamics of the Loop Current and the eddy shedding (Fig. 5). This indicates that baroclinic instability is not an essential element of the dynamics. Instead a horizontal shear instability of the first internal mode (a barotropic instability) is the dominant instability mechanism.

3) We have demonstrated the usefulness of CAV trajectory analysis and internal Rossby waves in explaining the eddy-shedding behavior of the Loop Current, including the eddy diameter, the Loop Current penetration into the Gulf, the latitude of westward bending by the Loop Current, the westward speed of eddy propagation, and the eddy shedding period (see Table 2). The role of differential rotation (β) is pervasive. This theory also showed that it is not necessary to invoke an instability mechanism to explain the westward bending of the Loop Current, nor the tendency for it to loop back on itself. This suggests that an instability may be essential only to explain the final eddy separation from the Loop Current.

4) Two steady regimes were found in the parameter space neighboring the eddy shedding regime. The parameter space occupied by each regime was depicted on a regime diagram for the reduced gravity model (Fig. 10).

5) In the presence of sufficient deep water inflow through the Yucatan Straits, the Florida Shelf topography may prevent Loop Current penetration, westward bending and eddy shedding by effectively reducing the port separation. This shifts the

Loop Current into one of the stable regimes (Section 7). Certain time variations in the deep flow through the Yucatan Straits may have a greater effect on the Loop Current than fluctuations in the upper layer flow through the strait.

6) Bottom topography plays another important role by inhibiting baroclinic instability. Thus the reduced gravity solutions were more like two-layer solutions with the idealized Gulf of Mexico topography (Fig. 3) than two-layer flat-bottom solutions. The topography also demonstrated some ability to steer eddies in the upper ocean through back interaction from eddies in the lower layer which were mostly confined to the abyssal plain.

7) Finally, we examined the characteristic signatures of barotropic and baroclinic instability in the pressure fields of both layers and in the eddy-mean energetics. In both cases there was a tendency for eddies in the upper layer to drive a modon in the lower layer. The upper and lower layer phase relations were surprisingly similar for both types of instability, but the westward propagation speeds associated with baroclinic instability were typically two to three times faster.

ACKNOWLEDGEMENTS

We extend our appreciation to Dr. L. B. Lin, who developed much of the analysis and display software, including the eddy-mean energetics. We thank Ruth Preller, John Harding, Monty Peffley, Marla Burson and Cynthia Seay for assisting us in various aspects of manuscript preparation. Dr. Daniel Moore of Imperial College, London provided the fast vectorized Helmholtz solvers for both rectangular and irregular domains. The CAV trajectory program was provided by Dr. Donna Blake. Some of the graphics software was supplied by the National Center for Atmospheric Research, which is sponsored by the National Science Foundation. Computations were performed on the two-pipeline Texas Instruments Advanced Scientific Computer at the Naval Research Laboratory in Washington, D.C. We thank Charlene Parker for typing the manuscript.

APPENDIX A

List of Symbols

A	horizontal eddy viscosity
c_{ir}	nondispersive internal Rossby wave speed
c_r	internal Rossby wave speed including dispersion
E_B	beta Ekman number, $A/(BL_p^3)$
f, f_0	Coriolis parameter; f_0 taken at southern boundary (y_0)
g	acceleration due to gravity
g'	reduced gravity, $g(\rho_2 - \rho_1)/\rho$
$H_1, H_2(x,y)$	initial thicknesses of the layers
h_1, h_2	instantaneous local thickness of the layers

K_i, \bar{K}_i, K'_i	kinetic energy $\frac{1}{2}(u^2 + v^2)$; of the mean flow; mean of the eddy flow, respectively, for layer i .
k, ℓ	zonal and meridional wave numbers, respectively
L	halfwidth of the southern port
L_{BF}	minimum frictional length scale over which β is important, $(A/\beta)^{1/3}$
L_{BI}	minimum inertial length scale over which β is important, $(v_c/\beta)^{1/2}$
L_{np}	maximum northward penetration of the Loop Current
L_p	half the port separation distance
P, \bar{P}, P'	potential energy $\frac{1}{2}\rho(gn_1^2 + g'n_2^2)$; of the mean flow; mean of the eddy flow, respectively.
p_1	upper layer density-normalized pressure, gn_1 .
p_2	lower layer density-normalized pressure, $gn_1 - g'(h_1 - H_1)$
Pe	eddy shedding period
R_B	beta Rossby number, $v_c/\beta L_p^2$
Re	Reynolds number, $v_c L/A$
r	eddy radius
t	time
Δt	time increment in the numerical integration
u_1, u_2	x-directed components of current velocity
v_{ci}	maximum inflow speed
v_c	speed at the core of the current
v_g	geostrophic meridional transport
w_1, w_2	$h_1 w_1, h_2 w_2$
x, y, z	tangent plane Cartesian coordinates: x positive eastward, y positive northward, z positive upward
x_L, y_L	east-west and north-south domain size
$\Delta x, \Delta y$	horizontal grid increments
β	differential rotation, df/dy
ζ	relative vorticity $v_x - u_y$
η_1	free surface anomaly; height of the free surface above its initial uniform elevation; $\eta_1 = h_1 + h_2 - H_1 - H_2$
η_2	$\eta_2 = H_1 + \eta_1 - h_1 = h_2 - H_2 = -PA$
θ_I	angle of inflow with respect to the positive x -axis
λ	internal radius of deformation
ρ, ρ_1, ρ_2	densities of sea water
τ_i^x, τ_i^y	x and y directed tangential stresses at the top (i) and bottom ($i + 1$) of layer i

APPENDIX B

New Reduced Gravity Experiments for the Regime Diagram (Fig. 10)

Experiment	v_{ci}	L	A	L_p	β	Re	R_B	Regime
155	54.4	80	4.0	227.1	2.0	10.9	.527	W
157	54.1	80	4.0	150.9	2.0	10.8	1.19	M
158	73.4	80	2.0	203.5	2.0	29.4	.89	E
159	73.2	80	2.5	203.5	2.0	23.4	.88	T
160	40.3	80	7.3	203.5	.49	4.4	1.99	N
161	41.4	80	1.6	203.5	.537	20.7	1.86	M
162	41.2	80	1.6	203.5	.69	20.6	1.44	W
163	40.5	80	4.6	203.5	1.21	7.0	.81	M
164	40.8	80	4.6	203.5	.69	7.1	1.43	N

units: v_{ci} in cm/s; L, L_p in km; A in $10^7 \text{ cm}^2/\text{s}$; β in $10^{-13} \text{ cm}^{-1} \text{ sec}^{-1}$

See Appendix A for symbol definitions. Note that L and L_p are the half-port width and half-port separation, respectively. The other parameters are the same as in Table 1 except that (1) in Experiments 155 and 157 a land mass was inserted in the location of the West Florida Shelf (See Fig. 9b, c) and the center of the eastern port was taken to be 75 km south of the western end of this land mass, (2) the southern port was centered at $x_p = 1000$ km in Experiment 155 and at $x_p = 1160$ km in Experiment 157, and (3) the inflow transport was 14 Sv in Experiments 155 and 157, and 10 Sv in Experiments 160-164.

APPENDIX C

Derivation of Eddy-mean Energetics for a Two-layer, Free-surface, Primitive-equation Model with Open Boundaries

Consider the momentum form of the primitive equations for a two-layer fluid with a free surface:

$$\frac{\partial w_i}{\partial t} + w_i \cdot \nabla w_i + \hat{k} \times f w_i = -\nabla p_i + (\epsilon_i - \epsilon_{i+1})/(\rho h_i) + A \nabla^2 w_i \quad (C1)$$

$$\frac{\partial \eta_1}{\partial t} + \nabla \cdot (h_1 w_1 + h_2 w_2) = 0 \quad (C2)$$

$$\frac{\partial \eta_2}{\partial t} + \nabla \cdot (h_2 w_2) = 0 \quad (C3)$$

where $i=1,2$ and η_1 and η_2 are the deviations of the free surface and the interface, respectively (see Appendix A). Also,

$$p_1 = gn_1$$

$$g' = g(\rho_2 - \rho_1)/\rho$$

$$p_2 = p_1 - g'(\eta_1 - \eta_2)$$

$$\tau_i = \tau_i^x \hat{i} + \tau_i^y \hat{j}$$

Note in (C1) that we have used the traditional form of Laplacian friction.

Now define the kinetic and potential energies as

$$\begin{aligned} K_i &= \frac{1}{2} \rho h_i (u_i^2 + v_i^2) \quad \text{where } i=1,2 \\ P &= \frac{1}{2} \rho (gn_1^2 + g'\eta_2^2). \end{aligned} \quad (C4)$$

Multiplying (C1) by $\rho h_i w_i$ ($i=1,2$) and using (C2) and (C3) we obtain the kinetic energy equations:

$$\begin{aligned} \frac{\partial K_1}{\partial t} + \nabla \cdot (w_1 K_1) + \rho g \nabla \cdot (h_1 w_1 \eta_1) \\ = \rho g \eta_1 \nabla \cdot (h_1 w_1) + \rho A h_1 w_1 \nabla^2 w_1 \end{aligned} \quad (C5)$$

and

$$\begin{aligned} \frac{\partial K_2}{\partial t} + \nabla \cdot (w_2 K_2) + \rho g \nabla \cdot (h_2 w_2 \eta_1) \\ + \rho g' \nabla \cdot (h_2 w_2 \eta_2) = \rho g \eta_1 \nabla \cdot (h_2 w_2) \\ + \rho g' \eta_2 \nabla \cdot (h_2 w_2) + \rho A h_2 w_2 \nabla^2 w_2 \end{aligned} \quad (C6)$$

Note that in deriving (C6) we have assumed $g' \nabla \eta_1 \ll g \nabla \eta_1$ and $\epsilon_i = 0$ for $i=1,2,3$. The potential energy equation is formed by multiplying (C2) by $\rho g \eta_1$ and (C3) by $\rho g' \eta_2$ and summing the results:

$$\frac{\partial P}{\partial t} + \rho g \eta_1 \nabla \cdot (h_1 w_1 + h_2 w_2) + \rho g' \eta_2 \nabla \cdot (h_2 w_2) = 0 \quad (C7)$$

Now define mean and perturbation quantities for u , v , h , and η such that

$$\overline{(\quad)} = \frac{1}{T} \int_{t_0}^{t_0+T} (\quad) dt$$

and

$$(\overline{\quad})' = (\quad) - (\overline{\quad}),$$

where T is a suitable time interval. Also define the kinetic energy of the mean flow per unit area as

$$\bar{K}_i = \frac{1}{2} \rho h_i (\bar{u}_i^2 + \bar{v}_i^2), \quad i=1,2 \quad (C8)$$

and the mean kinetic energy of the eddy flow per unit area as

$$\bar{K}_i' = \frac{1}{2} \rho h_i (\bar{u}_i'^2 + \bar{v}_i'^2) - \bar{K}_i. \quad (C9)$$

Similarly, for the potential energy of the mean flow

$$\bar{P} = \frac{1}{2} \rho (g \bar{n}_1^2 + g' \bar{n}_2^2) \quad (C10)$$

and for the mean potential energy of the eddy flow

$$\bar{P}' = \frac{1}{2} \rho (g \bar{n}_1'^2 + g' \bar{n}_2'^2) \quad (C11)$$

The \bar{K}_1 equation is obtained by multiplying (C1) with $i=1$ by $\rho \bar{h}_1 \bar{w}_1$:

$$\begin{aligned} \frac{\partial \bar{K}_1}{\partial t} = & - \nabla \cdot (\bar{w}_1 \bar{K}_1) - \gamma_1 - \rho g \nabla \cdot (\bar{n}_1 \bar{h}_1 \bar{w}_1) \\ & + \rho g \bar{n}_1 \nabla \cdot (\bar{h}_1 \bar{w}_1) + \rho A \bar{h}_1 \bar{w}_1 \bar{v}^2 \bar{w}_1 \end{aligned} \quad (C12)$$

where for layer i

$$\begin{aligned} \gamma_i = & \frac{1}{2} \rho (\bar{u}_i^2 + \bar{v}_i^2) \nabla \cdot (\bar{h}_i \bar{w}_i) + \rho \bar{h}_i \bar{u}_i (\nabla \cdot (\bar{u}_i \bar{w}_i)) \\ & - \bar{u}_i \nabla \cdot \bar{w}_i + \rho \bar{h}_i \bar{v}_i (\nabla \cdot (\bar{v}_i \bar{w}_i) - \bar{v}_i \nabla \cdot \bar{w}_i). \end{aligned}$$

The \bar{K}_1' equation is (C5) - (C12) or

$$\begin{aligned} \frac{\partial \bar{K}_1'}{\partial t} = & - [\nabla \cdot \bar{w}_1 \bar{K}_1 - \nabla \cdot (\bar{w}_1 \bar{K}_1)] + \gamma_1 \\ & - \rho g \nabla \cdot (\bar{n}_1 \bar{h}_1 \bar{w}_1 - \bar{n}_1 \bar{h}_1 \bar{w}_1) + \rho g \bar{n}_1 \nabla \cdot (\bar{h}_1 \bar{w}_1) \\ & - \bar{n}_1 \nabla \cdot (\bar{h}_1 \bar{w}_1) + \rho A (\bar{h}_1 \bar{w}_1 \bar{v}^2 \bar{w}_1 - \bar{h}_1 \bar{w}_1 \bar{v}^2 \bar{w}_1) \end{aligned} \quad (C13)$$

Similarly, for \bar{K}_2 and K'_2 we obtain

$$\begin{aligned}\frac{\partial \bar{K}_2}{\partial t} = & - \nabla \cdot (\bar{w}_2 \bar{K}_2) - \gamma_2 - \rho g \nabla \cdot (\bar{\eta}_1 \bar{h}_2 \bar{w}_2) \\ & + \rho g \bar{\eta}_1 \nabla \cdot (\bar{h}_2 \bar{w}_2) - \rho g' \nabla \cdot (\bar{\eta}_2 \bar{h}_2 \bar{w}_2) \\ & + \rho g' \bar{\eta}_2 \nabla \cdot (\bar{h}_2 \bar{w}_2) + \rho A \bar{h}_2 \bar{w}_2 \bar{v}^2 \bar{w}_2\end{aligned}\quad (C14)$$

and

$$\begin{aligned}\frac{\partial K'_2}{\partial t} = & - [\nabla \cdot (\bar{w}_2 \bar{K}_2) - \nabla \cdot (\bar{w}_2 \bar{K}_2)] + \gamma_2 \\ & - \rho g [\nabla \cdot (\bar{\eta}_1 \bar{h}_2 \bar{w}_2) - \nabla \cdot (\bar{\eta}_1 \bar{h}_2 \bar{w}_2)] \\ & + \rho g [\bar{\eta}_1 \nabla \cdot (\bar{h}_2 \bar{w}_2) - \bar{\eta}_1 \nabla \cdot (\bar{h}_2 \bar{w}_2)] \\ & - \rho g' [\nabla \cdot (\bar{\eta}_2 \bar{h}_2 \bar{w}_2) - \nabla \cdot (\bar{\eta}_2 \bar{h}_2 \bar{w}_2)] \\ & + \rho g' [\bar{\eta}_2 \nabla \cdot (\bar{h}_2 \bar{w}_2) - \bar{\eta}_2 \nabla \cdot (\bar{h}_2 \bar{w}_2)] \\ & + \rho A [\bar{h}_2 \bar{w}_2 \bar{v}^2 \bar{w}_2 - \bar{h}_2 \bar{w}_2 \bar{v}^2 \bar{w}_2]\end{aligned}\quad (C15)$$

The \bar{P} equation is obtained by multiplying (C2) by $\rho g \bar{\eta}_1$ and (C3) by $\rho g' \bar{\eta}_2$ and summing the results:

$$\begin{aligned}\frac{\partial \bar{P}}{\partial t} = & - \rho g \bar{\eta}_1 \nabla \cdot (\bar{h}_1 \bar{w}_1 + \bar{h}_2 \bar{w}_2) - \rho g \bar{\eta}_1 \nabla \cdot (\bar{h}_1' \bar{w}_1' + \bar{h}_2' \bar{w}_2') \\ & - \rho g' \bar{\eta}_2 \nabla \cdot (\bar{h}_2 \bar{w}_2) - \rho g' \bar{\eta}_2 \nabla \cdot (\bar{h}_2' \bar{w}_2')\end{aligned}\quad (C16)$$

By subtracting (C16) from (C7), we obtain the P' equation:

$$\begin{aligned}\frac{\partial P'}{\partial t} = & - \rho g [\bar{\eta}_1 \nabla \cdot (\bar{h}_1 \bar{w}_1 + \bar{h}_2 \bar{w}_2) - \bar{\eta}_1 \nabla \cdot (\bar{h}_1' \bar{w}_1' + \bar{h}_2' \bar{w}_2')] \\ & + \rho g \bar{\eta}_1 \nabla \cdot (\bar{h}_1' \bar{w}_1' + \bar{h}_2' \bar{w}_2') \\ & - \rho g' [\bar{\eta}_2 \nabla \cdot (\bar{h}_2 \bar{w}_2) - \bar{\eta}_2 \nabla \cdot (\bar{h}_2' \bar{w}_2')] \\ & + \rho g' \bar{\eta}_2 \nabla \cdot (\bar{h}_2' \bar{w}_2')\end{aligned}\quad (C17)$$

When the terms in the energy equations are calculated from a model solution in statistical equilibrium and a suitable time average is used, the tendency terms are negligible. Regional energy budgets can be obtained, if (C12) - (C17) are also integrated spatially. Integrated over a closed basin the divergence terms vanish, but in an open domain they must be retained. The energy balances are conveniently displayed using an energy box diagram such as Fig. 12a. Each term is represented by an arrow in or out of the box for the energy reservoir associated with that equation. When identical terms with opposite sign appear in two equations, they represent a conversion of energy from one type to another. The energy transfers shown in Fig. 12a were calculated from the spatially integrated terms in (C12) - (C17) as shown below.

\bar{K}_1 terms

$$\begin{aligned}
 \{\bar{K}_1 F \rightarrow \bar{K}_1\} &\equiv - \iint \nabla \cdot (\bar{w}_1 \bar{K}_1) dx dy \\
 \{\bar{K}_1 \rightarrow K'_1\} &\equiv \iint Y_1 dx dy \\
 \{PW \rightarrow \bar{K}_1\} &\equiv - \rho g \iint \nabla \cdot (\bar{\eta}_1 \bar{h}_1 \bar{w}_1) dx dy \\
 \{\bar{K}_1 \rightarrow \bar{P}\} &\equiv - \rho g \iint \bar{\eta}_1 \nabla \cdot (\bar{h}_1 \bar{w}_1) dx dy \\
 \{\bar{K}_1 \rightarrow D\} &\equiv - \rho A \iint \bar{h}_1 \bar{w}_1 \nabla^2 \bar{w}_1 dx dy
 \end{aligned} \tag{C18}$$

K'_1 terms

$$\begin{aligned}
 \{K'_1 F \rightarrow K'_1\} &\equiv - \iint \nabla \cdot (\bar{w}_1 \bar{K}_1 - \bar{w}_1 \bar{K}_1) dx dy \\
 \{\bar{K}_1 \rightarrow K'_1\} &\equiv \iint Y_1 dx dy \\
 \{PW \rightarrow K'_1\} &\equiv - \rho g \iint \nabla \cdot (\bar{\eta}_1 \bar{h}_1 \bar{w}_1 - \bar{\eta}_1 \bar{h}_1 \bar{w}_1) dx dy \\
 \{K'_1 \rightarrow P'\} &\equiv - \rho g \iint [\bar{\eta}_1 \nabla \cdot (\bar{h}_1 \bar{w}_1) - \bar{\eta}_1 \nabla \cdot (\bar{h}_1 \bar{w}_1)] dx dy \\
 \{K'_1 \rightarrow D\} &\equiv - \rho A \iint [\bar{h}_1 \bar{w}_1 \nabla^2 \bar{w}_1 - \bar{h}_1 \bar{w}_1 \nabla^2 \bar{w}_1] dx dy
 \end{aligned} \tag{C19}$$

\bar{K}_2 terms

$$\begin{aligned}
 \{\bar{K}_2 F \rightarrow \bar{K}_2\} &\equiv - \iint \nabla \cdot (\bar{w}_2 \bar{K}_2) dx dy \\
 \{\bar{K}_2 \rightarrow K'_2\} &\equiv \iint \gamma_2 dx dy \\
 \{PW \rightarrow \bar{K}_2\} &\equiv - \rho \iint \nabla \cdot [(g\bar{\eta}_1 + g'\bar{\eta}_2) \bar{h}_2 \bar{w}_2] dx dy \\
 \{\bar{K}_2 \rightarrow \bar{P}\} &\equiv - \rho \iint (g\bar{\eta}_1 + g'\bar{\eta}_2) \nabla \cdot (\bar{h}_2 \bar{w}_2) dx dy \\
 \{\bar{K}_2 \rightarrow D\} &\equiv - \rho A \iint \bar{h}_2 \bar{w}_2 \nabla^2 \bar{w}_2 dx dy
 \end{aligned} \tag{C20}$$

K'_2 terms

$$\begin{aligned}
 \{K'_2 F \rightarrow K'_2\} &\equiv - \iint \nabla \cdot (\bar{w}_2 \bar{K}_2 - \bar{w}_2 \bar{K}'_2) dx dy \\
 \{\bar{K}_2 \rightarrow K'_2\} &\equiv \iint \gamma_2 dx dy \\
 \{PW \rightarrow K'_2\} &\equiv - \rho \iint \nabla \cdot [(\bar{g}\bar{\eta}_1 + \bar{g}'\bar{\eta}_2) \bar{h}_2 \bar{w}_2 - (g\bar{\eta}_1 + g'\bar{\eta}_2) \bar{h}_2 \bar{w}_2] dx dy \\
 \{K'_2 \rightarrow P'\} &\equiv - \rho \iint [(\bar{g}\bar{\eta}_1 + \bar{g}'\bar{\eta}_2) \nabla \cdot (\bar{h}_2 \bar{w}_2) - (g\bar{\eta}_1 + g'\bar{\eta}_2) \nabla \cdot (\bar{h}_2 \bar{w}_2)] dx dy \\
 \{K'_2 \rightarrow D\} &\equiv - \rho A \iint [\bar{h}_2 \bar{w}_2 \nabla^2 \bar{w}_2 - \bar{h}_2 \bar{w}_2 \nabla^2 \bar{w}_2] dx dy
 \end{aligned} \tag{C21}$$

\bar{P} terms

$$\begin{aligned}
 \{\bar{K}_1 \rightarrow \bar{P}\} &\equiv - \rho g \iint \bar{\eta}_1 \nabla \cdot (\bar{h}_1 \bar{w}_1) dx dy \\
 \{\bar{P} \rightarrow \bar{K}_2\} &\equiv \rho \iint (g\bar{\eta}_1 + g'\bar{\eta}_2) \nabla \cdot (\bar{h}_2 \bar{w}_2) dx dy \\
 \{\bar{P} \rightarrow P'\} &\equiv \rho \iint [g\bar{\eta}_1 \nabla \cdot (\bar{h}_1' \bar{w}_1' + \bar{h}_2' \bar{w}_2') + g'\bar{\eta}_2 \nabla \cdot (\bar{h}_2' \bar{w}_2')] dx dy
 \end{aligned} \tag{C22}$$

P' terms

$$\begin{aligned}
 \{K'_1 \rightarrow P'\} &\equiv - \rho g \iint [\bar{\eta}_1 \nabla \cdot (\bar{h}_1 \bar{w}_1) - \bar{\eta}_1 \nabla \cdot (\bar{h}_1 \bar{w}_1)] dx dy \\
 \{P' \rightarrow K'_2\} &\equiv \rho \iint [(\bar{g}\bar{\eta}_1 + \bar{g}'\bar{\eta}_2) \nabla \cdot (\bar{h}_2 \bar{w}_2) - (g\bar{\eta}_1 + g'\bar{\eta}_2) \nabla \cdot (\bar{h}_2 \bar{w}_2)] dx dy \\
 \{\bar{P} \rightarrow P'\} &\equiv \rho \iint [g\bar{\eta}_1 \nabla \cdot (\bar{h}_1' \bar{w}_1' + \bar{h}_2' \bar{w}_2') + g'\bar{\eta}_2 \nabla \cdot (\bar{h}_2' \bar{w}_2')] dx dy
 \end{aligned} \tag{C23}$$

The bracket notation is dropped in Section 8. In our results $|\bar{K}_1 \rightarrow K'_1| \gg |K'_1 F \rightarrow K'_1 + PW \rightarrow K'_1|$. Thus, any controversy over the formulation of these terms (Harrison and Robinson, 1978) should not cloud the interpretation of the basic results in Fig. 12. Also, the difference between the frictional formulation in the models and the energetics did not result in any serious imbalances in the energy equations.

REFERENCES

Blumberg, A. F. and G. L. Mellor, 1981: A numerical calculation of the circulation in the Gulf of Mexico. Dynalysis of Princeton Rept. No. 66. Prepared for Division of Solar Technology. U.S. Dept. of Energy., 159 pp.

Cochrane, J. D., 1965: The Yucatan Current and equatorial currents of the western Atlantic, Unpublished report, Dept. of Oceanography, Texas A&M University, Ref. (65-17T), 20-27.

Elliott, B. A., 1979: Anticyclonic rings and the energetics of the circulation of the Gulf of Mexico. Ph.D. thesis, Dept. of Oceanography, Texas A&M University, 188 pp.

Gill, A. E., J. S. A. Green, and A. J. Simmons, 1974: Energy partition in the large-scale ocean circulation and the production of mid-ocean eddies. Deep-Sea Research, 21, 499-528.

Haltiner, G. J., and F. L. Martin, 1957: Dynamical and Physical Meteorology, McGraw-Hill, 470 pp.

Harrison, D. E., and A. R. Robinson, 1978: Energy analysis of open regions of turbulent flows-mean eddy energetics of a numerical ocean circulation experiment. Dyn. Atmos. Oceans, 2, 185-211.

Holland, W. R., and L. B. Lin, 1975: On the generation of mesoscale eddies and their contribution to the oceanic general circulation. I. A preliminary numerical experiment. J. Phys. Oceanogr., 5, 642-657.

Hurlburt, H. E. and J. D. Thompson, 1980: A numerical study of Loop Current intrusions and eddy shedding. J. Phys. Oceanogr., 10, 1611-1651.

Leipper, D. F., 1970: A sequence of current patterns in the Gulf of Mexico. J. Geophys. Res., 75, 637-657.

McWilliams, J. C., and G. R. Flierl, 1979: On the evolution of isolated, nonlinear vortices. J. Phys. Oceanogr., 9, 1155-1182.

Nowlin, W. D., 1972: Winter circulation patterns and property distributions. Contributions on the Physical Oceanography of the Gulf of Mexico, Vol. II, L. R. A. Capurro and J. L. Reid, Eds., Gulf Publishing Co., 3-51.

Pedlosky, J., 1979: Geophysical Fluid Dynamics, Springer-Verlag. 624 pp.

Philander, S. G. H., 1976: Instabilities of zonal equatorial currents. J. Geophys. Res., 81, 3725-3735.

Reid, R. O., 1972: A simple dynamic model of the Loop Current. Contributions on the Physical Oceanography of the Gulf of Mexico, Vol. II, L. R. A. Capurro and J. L. Reid, Eds., Gulf Publishing Co., 157-159.

Rhines, P., 1977: The dynamics of unsteady currents. The Sea, Vol. 6, E. D. Goldberg, I. N. McCave, J. J. O'Brien and J. H. Steele, Eds., Wiley Interscience, 189-318.

Rossby, C. G., 1940: Planetary flow patterns in the atmosphere. Quart. J. Roy. Meteor. Soc., 66 (Suppl.), 68-87.

UNCLASSIFIED

SECURITY CLASSIFICATION OF THIS PAGE (When Data Entered)

REPORT DOCUMENTATION PAGE		READ INSTRUCTIONS BEFORE COMPLETING FORM
1. REPORT NUMBER	2. GOVT ACCESSION NO.	3. RECIPIENT'S CATALOG NUMBER
NORDA Technical Note 125		AD-A114 362
4. TITLE (and Subtitle) The Dynamics of the Loop Current and Shed Eddies in a Numerical Model of the Gulf of Mexico		5. TYPE OF REPORT & PERIOD COVERED
		6. PERFORMING ORG. REPORT NUMBER
7. AUTHOR(s) Harley E. Hurlburt J. Dana Thompson		8. CONTRACT OR GRANT NUMBER(s)
9. PERFORMING ORGANIZATION NAME AND ADDRESS Numerical Modeling Division Naval Ocean Research and Development Activity NSTL Station, Mississippi 39529		10. PROGRAM ELEMENT, PROJECT, TASK AREA & WORK UNIT NUMBERS
11. CONTROLLING OFFICE NAME AND ADDRESS		12. REPORT DATE October 1981
		13. NUMBER OF PAGES 55
14. MONITORING AGENCY NAME & ADDRESS (if different from Controlling Office)		15. SECURITY CLASS. (of this report) UNCLASSIFIED
		15a. DECLASSIFICATION/DOWNGRADING SCHEDULE
16. DISTRIBUTION STATEMENT (of this Report) Unlimited		
DISTRIBUTION STATEMENT A Approved for public release; Distribution Unlimited		
17. DISTRIBUTION STATEMENT (of the abstract entered in Block 20, if different from Report)		
18. SUPPLEMENTARY NOTES		
19. KEY WORDS (Continue on reverse side if necessary and identify by block number) Baroclinic Instability Eddy Shedding Modon Generation Barotropic Instability Energetics, Eddy-mean Numerical Model, Gulf of Circulation, Gulf of Gulf of Mexico Mexico Mexico Loop Current Rings in Gulf of Mexico Eddies, Mesoscale Mesoscale Eddies Topography, Influente on Currents		
20. ABSTRACT (Continue on reverse side if necessary and identify by block number) The dynamics of the circulation in the Gulf of Mexico have been investigated using simple, efficient numerical models capable of simulating consistently observed dynamical features, including the Loop Current and the shedding of large anticyclonic eddies from the Loop. Over 150 model experiments were integrated to statistical equilibrium, typically 3-5 years. One popular hypothesis holds that the Loop Current sheds anticyclonic eddies in response to annual variations in the inflow through the Yucatan Straits.		

UNCLASSIFIED

SECURITY CLASSIFICATION OF THIS PAGE (When Data Entered)

However, a striking result from the models is their ability to simulate the observed quasi-annual eddy shedding period with no time variations in the inflow. The model-predicted eddy diameters, amplitudes, and westward propagation speeds are also realistic. The dominant instability mechanism in the eddy shedding is a horizontal shear instability of the first internal mode, a barotropic rather than a baroclinic instability. Therefore, a reduced-gravity model with one vertical mode is able to simulate the basic dynamics of the Loop Current-eddy system. Rossby-wave theory and a conservation of absolute vorticity trajectory analysis were used to explain the behavior of the Loop Current, including its northward penetration into the Gulf, the latitude of westward bending, the shedding period for the eddies, as well as their diameter, and their westward propagation speed.

A regime diagram for the reduced-gravity model was constructed in terms of the Reynolds number Re and the beta Rossby number $R_B = v_c / \beta L_p^2$, where v_c is the velocity at the core of the current, L_p is half the port separation distance, and β is the differential rotation. Eddy shedding can be prevented by reducing Re or by increasing R_B .

Bottom relief acts to inhibit baroclinic instability, yielding solutions more closely resembling those from the reduced-gravity model than the two-layer flat-bottom model. Topography also influences the paths of the shed eddies and, in the presence of sufficient deep water inflow through the Yucatan Straits, prevents Loop Current penetration, westward bending, and eddy shedding. In effect, the West Florida Shelf acts to reduce the port separation, increase R_B , and shift the Loop Current into a stable regime.

The signatures of barotropic and baroclinic instabilities in the two-layer Gulf of Mexico model were studied using upper and lower layer pressure fields and eddy-mean energetics. Both instability processes tend to drive a deep flow characterized by modon generation and they exhibit similar vertical phase relationships. However, in these experiments the westward propagation speeds associated with baroclinic instability are typically two to three times faster.

UNCLASSIFIED

SECURITY CLASSIFICATION OF THIS PAGE (When Data Entered)

